SPECTROSCOPIC ANALYSIS

OF

SELECTED SILICON CERAMICS

A Thesis Submitted to the College of

Graduate Studies and Research

In Partial Fulfillment of the Requirements

For the Degree of Master of Science

in the Department of Physics

University of Saskatchewan

Saskatoon

By

Sam Leitch

Keywords: soft x-ray spectroscopy, synchrotron radiation, silicon nitride, silicon oxynitride, density of states, electronic structure

PERMISSION TO USE

In presenting this thesis in partial fulfilment of the requirements for a Postgraduate degree from the University of Saskatchewan, I agree that the Libraries of this University may make it freely available for inspection. I further agree that permission for copying of this thesis in any manner, in whole or in part, for scholarly purposes may be granted by the professor or professors who supervised my thesis work or, in their absence, by the Head of the Department or the Dean of the College in which my thesis work was done. It is understood that any copying or publication or use of this thesis or parts thereof for financial gain shall not be allowed without my written permission. It is also understood that due recognition shall be given to me and to the University of Saskatchewan in any scholarly use which may be made of any material in my thesis.

Requests for permission to copy or to make other use of material in this thesis in whole or part should be addressed to:

Head of the Department of Physics and Engineering Physics

University of Saskatchewan

Saskatoon, Saskatchewan (S7N 5E2)

ABSTRACT

Silicon ceramics are popular in both commercial applications and material research. The purpose of this thesis is to present measurements and analysis of four different silicon ceramics: α, β and γ phases of silicon nitride and silicon oxynitride using soft x-ray spectroscopy, which analyses the electronic structure of materials by measuring the absorption and emission of x-ray radiation. Absorption and emission spectra of these materials are presented, many of which have not be previously documented. The results are compared to model spectra and together they provide information about the electronic structure of the material.

Assignments of emission features to element, orbital, and site symmetry are performed for each material. Combinations of silicon and nitrogen emission spectra provide insight into the strained bonding structure of nitrogen. It is concluded that p-dπ interaction plays a role in the bonding arrangement of nitrogen and oxygen sites within these structures. The emission features of non-equivalent silicon sites within γ-Si_3N_4 are identified, which represents some of the first analysis of same element, non-equivalent sites in a material.

Silicon absorption and emission spectra were plotted on the same energy scale to facilitate measurement of the band gap. Since previously measured band gaps are not well represented in literature, the measured band gaps were compared to values predicted using DFT calculations. The band gap values are in reasonable agreement to calculated values, but do not vary as widely as predicted.

ACKNOWLEDGEMENTS

I would like to thank all the people that helped me through this process. I want to thank my parents and family both pushing me when I needed a push. I want to thank Cara for putting up with me when I was pushed too hard. I want to thank the entire beamteam group for their collaboration and camaraderie. I especially want to thank my supervisor, Alexander Moewes for giving me the opportunity to pursue this research. Without his support, none of this would be possible. Work at the Advanced Light Source at Lawrence Berkeley National Laboratory is supported by the US Department of Energy (Contract DE-AC03-76SF00098). Alexander Moewes is a Canada Research Chair.

TABLE OF CONTENTS

LIST OF FIGURES

LIST OF TABLES

LIST OF ABBREVIATIONS

LPDOS	localized partial density of states
SXS	soft x-ray spectroscopy
XAS	x-ray absorption spectroscopy
XES	x-ray emission spectroscopy
CB	conduction band
VB	valence band
RIXS	resonant inelastic x-ray spectroscopy
ARPES	angular resolved photo-emission spectroscopy
DFT	density functional theory
OLCAO	orthogonal linear combination of atomic orbitals
LAPW+LO	linear augmented plane wave with local orbitals
XANES	x-ray absorption near-edge spectrum
TEY	total elector yield measurement
TFY	total fluorescent yield measurement
PFY	partial fluorescent yield measurement
MCD	multi-channel detector
CVD	chemical vapour deposition
MNOS	metal-nitride-oxide-semiconductor
Si_{tet}	tetrahedral coordinated silicon
Si_{oct}	octahedral coordinated silicon

1 INTRODUCTION

Ceramics are quite common in material research and development. They are formed by taking simple elements or molecular compounds and subjecting them to intense heat and pressure. By adjusting the ratio of the components as well as the heat and pressure applied, different materials can be produced with unique electrical and mechanical properties. The ability to "tune" the electrical and mechanical properties of a material makes ceramics useful for a wide range of applications. They can be found in mechanical applications such as cutting blades, packaging, and structural components, as well as electrical applications such as integrated circuits, lasers, and other optoelectronics.

The most well know material used in integrated circuits is silicon. Pure silicon is a semiconductor that when doped and configured in the proper geometry, produces a wide variety of integrated electronic devices. Although pure silicon not strictly a silicon ceramic, it serves as a basis for the other materials discussed in this thesis. Silicon and doped silicon have been thoroughly discussed in literature for many years, including both theoretical calculations of the electronic properties such as optical properties and electronic structure done by Joseph Mullaney,[1] and experimental analysis such as band mapping done by Luning et al.[2] Recent literature has focussed on using nanoscale properties of silicon. By confining silicon to quantum sized nanostructures, the optical and electronic properties can be further tuned to meet the needs of designers.[3-5]

Because silicon is widely used in the electronics industry, researchers have also attempted to develop ceramics that use silicon as a base. One of the widely studied silicon ceramics is silicon nitride. In the late 50s, studies of silicon nitride revealed that it could

exist in two different crystal structures.[6-8] The two materials were designated α-Si_3N_4 and β-Si_3N_4 based on the energy required to form them. At the time, it was determined that these two phases were functionally identical. However, further analysis with more accurate equipment revealed distinctly different mechanical and electronic properties, and they have been compared and contrasted ever since.[9-20]

More recently, a third crystalline phase of Si_3N_4 was discovered, designated γ-Si_3N_4.[21] This third phase has a cubic spinel structure, where silicon atoms take up both tetrahedral and octahedral cation sites. The octahedrally coordinated Si in this structure is unique to nitrogen ceramics and serves to increase the hardness of the material as well as to reduce the band gap. There are also theoretical studies into what other materials could be created with this spinel structure.[22, 23] Although there are a large number of publications on the physical properties on γ-Si_3N_4,[24-27] studies of the electronic properties of this material are relatively scarce.[28, 29]

Silicon oxynitride is another material that has been under investigation in literature. Si_2N_2O can be considered an intermediate crystal structure between Si_3N_4 and SiO_2, only varying from the crystal structure of α-Si_3N_4 to account for the inclusion of O atoms. Si_2N_2O is considered a promising candidate for electro-optics and organic light-emitting devices.[30, 31] Since the benefits of Si_2N_2O have not been realized until recently, there are very few publications on the optical and electronic properties of this material as well.[32]

The purpose of this thesis is to compare and contrast results of x-ray spectroscopic data taken for these four silicon ceramics: α-Si_3N_4, β-Si_3N_4, γ-Si_3N_4 and Si_2N_2O. X-ray

absorption and emission spectra for all transition energies within the range of beamline 8.0.1 at the Advanced Light Source are presented, many of which have not been previously published. Comparison of the x-ray absorption and emission spectra with calculated spectra will be used to probe the electronic structure of each material based on element, orbital symmetry, and local geometry. The bonding structure of the materials will be analyzed as it relates to element, site and orbital symmetries. Finally, by combining the absorption and emission on the same energy scale, a band gap measurement for each material will be determined. Since determining the band gap using x-ray emission and absorption is not widely used, the advantages and disadvantages will be discussed which provide uncertainty in the measurement. Since measured band gaps of these materials are not well represented in literature, the band gaps will be compared to calculated band gaps obtained using density functional theory.

2 METHODS/THEORY

2.1 Soft X-ray Spectroscopy

Soft x-ray spectroscopy utilizes electron excitation to analyze materials.[33] Photons in the soft x-ray energy region (50 eV – 10 keV) excite electrons from low-lying core states to unoccupied conduction band (CB) states. The absorption and subsequent emission of photons produce distinctive energy dispersive spectra.

Soft x-ray emission and absorption spectroscopy have many useful properties that make it a powerful tool in the field of materials research. SXS is element specific, since different elements have different core-CB transition energies that rarely overlap. It is bulk-sensitive, since soft x-rays have a penetration depth of 10-100 nm well beyond the range of surface-sensitive states. Core orbitals are highly localized so it provides only information surrounding individual atomic sites. Lastly, only states that follow a specific orbital symmetry will be measured since the process is dipole in nature, following selection rule $\Delta l=\pm 1$ where l is the orbital quantum number.

When discussing soft x-ray spectra, we will quite often refer to the LPDOS or localized partial density of states. SXS deals with exciting electrons so the spectra produced are related to the density of electrons or electronic states in a given energy range. Since SXS is site specific, we are only interested in the electronic states localized around a single atomic site. SXS is also sensitive to atomic orbital symmetry so we are only interested in part of the total density of states surrounding the atom. SXS is therefore related to the localized partial density of states (LPDOS) surrounding a single atomic site within a given energy range.

X-ray absorption spectra (XAS) are produced when an electron is excited from a core hole to higher lying orbitals or, as in the case of light elements like Si and N, to the conduction band. Since core electrons are localized to their atomic sites and have atomic-like structure with well-known binding energy, the probability of absorption closely resembles the LPDOS of unoccupied states in the conduction band. By varying the excitation energy and measuring the rate of absorption, an XAS spectrum is obtained.

When an electron is excited to conduction band states, a core hole is left in the atom. The hole is filled with an electron from occupied valence band (VB) states. Among other non-radiative processes, the energy from this transition can be released by emitting a photon. Since low-lying core states have well-known energies, the emission spectrum resembles the LPDOS of occupied states below the Fermi level. This process is known as x-ray emission spectroscopy (XES).

X-ray emission is an improbable process, and requires long count times or high incident beam intensity to provide the required measurement statistics. For example, Si $L_{2,3}$ emission for Si with one 2p hole will occur with a probability 3.7-4.8 x 10^{-4}, while N K emission has a probability of 5.2 x 10^{-3}.[34] Resonant emission is used to combat this. By tuning the excitation energy to features in the XAS spectrum a resonant absorption/emission process is created, which produces a large number of core holes and therefore an increased emission intensity.

There is a separation commonly followed when discussing XES spectra that revolves around whether absorption and emission can be considered a single process or a combination of processes produced by independent states.[35] When absorption and

emission are considered separate processes, the system is allowed to remain in a pseudo-stable excited state for a finite amount of time. This is case for non-resonant excitation when the excitation energy is sufficiently above the ionization threshold. During that time, random phonon interactions alter the momentum of the core hole and the resulting emission process is considered to have random momentum. When we discuss XES spectra, we are generally referring to spectra that are produced through this two-step process.

Alternatively, resonant inelastic x-ray spectroscopy (RIXS) is the study of materials using combined excitation/emission process. The material absorbs a photon, and a second photon is emitted at a related energy without the appearance of a pseudo-stable intermediate state. Since photons transfer very little momentum to the system, the momentum during the combined absorption/emission process remains constant. RIXS measurement and analysis provides a greater degree of control for measurements, since both momentum and energy difference are known. The excitation energy of the system influences the emission spectrum of the material.

A further degree of control can be gained if the sample is a single crystal with known geometry. Angular resolved photoemission spectroscopy (ARPES) is a technique that uses photons to excite electrons out of a material into the continuum. When a single crystal sample is used, the momentum of emitted electrons is exactly known. Such angular resolved techniques can be used, in conjunction with RIXS, to map the complete band structure of materials. Unfortunately, new materials often require high temperature and pressure to synthesize and single crystal samples are rare.

2.2 Calculations

Our group has relied on collaborators to perform the complex density functional calculations required for theoretical comparison. In recent literature, one of the most published authors on the subject of simple structured ceramics (especially silicon ceramics) is Prof. Wai-Yim Ching at the University of Missouri - Kansas City. He has generously provided our group with calculated data that has proven profoundly informative and has become the basis for much of our data analysis.

Even though these calculations are not performed by our group it is important to have a strong understanding of what calculations can be performed and, most importantly, what limitations they have. Knowledge of the advantages and limitations of calculations allows comparisons of calculated and experimental results.

Much of the recent work in modelling solid-state systems has revolved around the use of density functional theory (DFT). For a more detailed analysis of DFT calculations, please refer to Appendix A. This calculation method involves taking the time averaged electron density for occupied states in the system, and minimizing the overall energy functional. This is generally accomplished by solving for a linear set of electron Schrödinger equations for electron-electron and electron-nuclear Coulomb potentials. To accomplish this, Prof. Ching's group uses the orthogonal linear combination of atomic orbitals method (OLCAO),[36] which uses a Bloch sum of atomic or atomic-like orbitals centred on atomic sites. By minimizing the energy functional of the orthogonal equations, the ground state energy eigenvalues and wave functions can be determined. From the wave

functions and corresponding eigenvalues, properties such as band structure and LPDOS can be derived.

Since Bloch sums are used in the analysis of the system, band structure is the most fundamental property obtained. The band-structure can then be further broken down, based on atomic, orbital and spin symmetries. LPDOS can then be derived based on the same criteria. An example of the unoccupied LPDOS of γ-Si_3N_4 with nitrogen p orbital symmetry is shown in Figure 2.1(a).

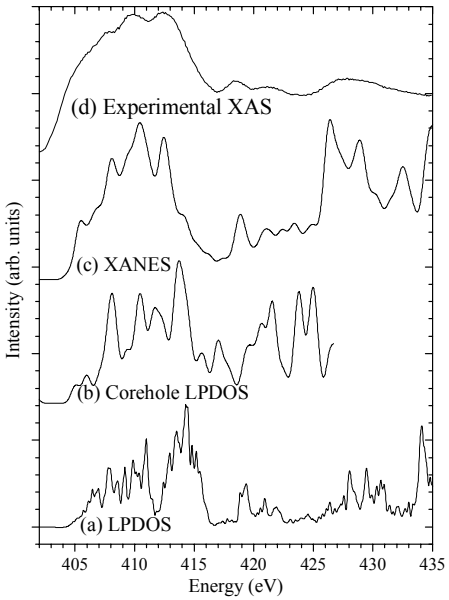

Figure 2.1: Comparison of progression of XAS spectrum in γ-Si_3N_4

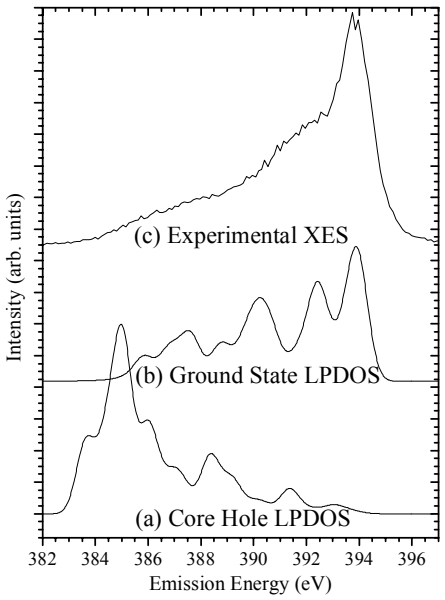

Figure 2.2: Comparison of different supercell atoms to XES spectrum in γ-Si_3N_4

LPDOS gives a basic trend for the experimental data, but lacks the effects of the core hole on the wave functions. The core hole left after an electron is excited to conduction band states will interact with and change the LPDOS surrounding that nucleus. To calculate the effects of core hole interaction, a supercell approach is used. Instead of

calculating wave functions for a single unit cell, a number of unit cells are combined, limited to ~100 atoms by the available computing power. An electron is removed from the core of a single atom in the supercell, and placed in the lowest unoccupied states. The wave functions of the new system are calculated, and the resulting LPDOS are derived. Figure 2.1(b) shows an example supercell LPDOS for an N atom in γ-Si_3N_4 with a 1s core hole.

The core hole included LPDOS more accurately represents the experimental absorption spectra, as it more accurately represents the availability of excitation states. However, this picture does not take into account variations in transition probability. The probability of exciting an electron from a core state to a conduction band state at a given energy is known as the transition probability. Using the same supercell approach, wave functions for both the initial and final states of the excited system can be performed. By including transition matrix elements, a complete quantum-mechanical interpretation of the x-ray absorption near-edge spectrum (XANES) is derived. Figure 2.1(c) shows the XANES for the same N K absorption of γ-Si_3N_4. This data can be directly compared to experimental data (Figure 2.1(d)), as it includes all major components of a quantum-mechanical interpretation of an x-ray absorption spectrum.

The final step in the process would be to model emission spectra based on excitation energy. Prof Ching's group does not currently do this type of calculation, but is in the works. In the meantime, LPDOS data is used for comparison.

It would seem most logical that the LPDOS that includes core hole interactions would be the closest representation of the emission spectrum, since it represents the wave function

of the atom with a core hole. Figure 2.2 shows (a) the LPDOS of N in γ-Si_3N_4 for the excited atom in a supercell, (b) The LPDOS of an atom that remains in the ground state in the same supercell, and (c) the experimental emission spectrum for comparison. The LPDOS of the two ground state and core hole N atoms are dramatically different and the ground states LPDOS appears to more accurately model the measured emission spectrum. This is counter-intuitive at first, and can be explained the same way as for absorption: the emission spectrum represents the final state of the system. In this case, the final state of the system is the ground state. All absorption/emission processes tend to exhibit properties of the final state of the system, as explained by Vonbarth et al.[37] This effect is known as the final state rule.

2.3 Broadening Factors

As with any kind of spectroscopic study, broadening factors in XES/XAS limit the accuracy and detail of analysis. However, broadening can also be used as a tool to learn new properties of a material that may otherwise be unobtainable. There are three broadening effects we take into account when modelling XES/XAS: Instrumental broadening, core hole lifetime broadening, and final state lifetime broadening. While these are not the only broadening effects involved in XAS/XES, these three factors have been isolated as the major and measurable causes of spectral broadening in these systems.

Instrumental broadening is a statistical process caused by the optics and the environment that measurements take place. Purity of sources, purity of optical components and duration and intensity of measurements all contribute to instrumental broadening. Instead of discussing in detail each effect and how much it contributes, they are generally lumped

into a single broadening factor called resolving power (E/ΔE). Instrumental broadening is gaussian in nature and is modeled in calculated spectra by a gaussian function with a standard deviation derived from the resolving power.

Core hole lifetime broadening is caused by the short lifetime of the core hole created in the photon absorption process. The short lifetime causes a broadening in the energy of the state based on the Heisenberg uncertainty principle. Core hole lifetime broadening is modeled using a lorentzian function with a constant broadening factor based on the documented lifetime of the core hole.[38]

Final state lifetime broadening is very similar to core hole lifetime broadening. It is a result of the limited lifetime of the system after absorption or emission. After absorption, there is an electron left in the conduction band. After emission, there is a hole left in the valence band. Each of these excited states has a limited lifetime before they decay by either radiative or non-radiative processes. This lifetime causes an uncertainty in that state's energy value, broadening its respective spectrum. Because different energy states have different average lifetimes, final state broadening is not constant over the spectral range. Final state lifetime broadening is also simulated with a lorentzian function with a broadening factor derived by Goodings and Harris[39] and given by:

$$\Delta(E) = W\left\{1 - \frac{E - E_0}{E_F - E_0}\right\}^2 \tag{2.1}$$

Where W defines the scale of the broadening, E_F is the Fermi energy, and E_0 is the energy at the bottom of the lowest conduction band. All our calculated XES spectra use this equation for final states broadening, with a broadening scale (W) of 1 for both Si and N.

Emission spectra used in this thesis have been broadened according to these three factors. This was accomplished by taking the combined valence band LPDOS for each material based on the element and orbital symmetries measured and applying both a gaussian and lorentzian broadening routine I developed for Origin® using the previously discussed values as inputs. Calculated XANES spectra used in this discussion have been previously broadened by a constant gaussian function, which is sufficient for the purpose of comparison.

2.4 ALS Beamline 8.0.1

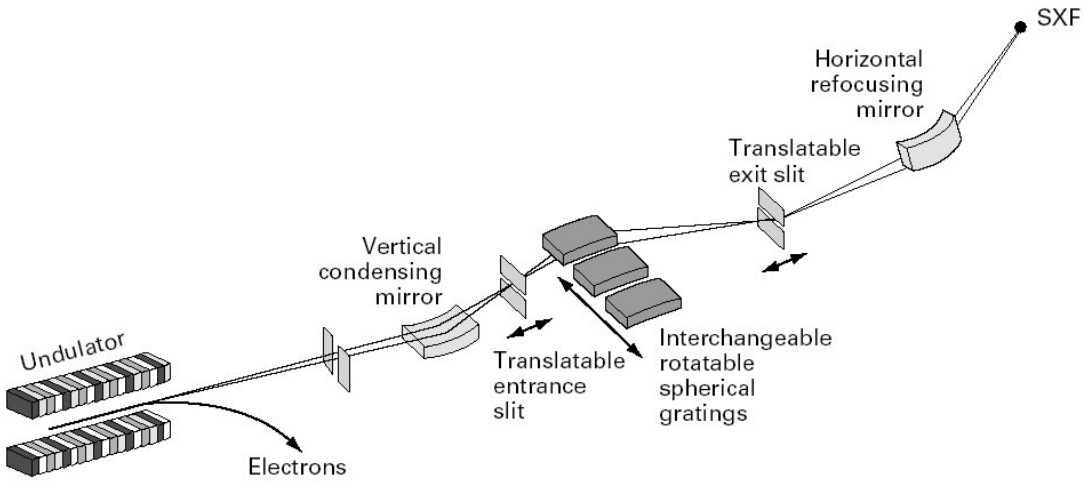

Figure 2.3: Schematic overview of undulator beamline 8.0 at ALS.[40]

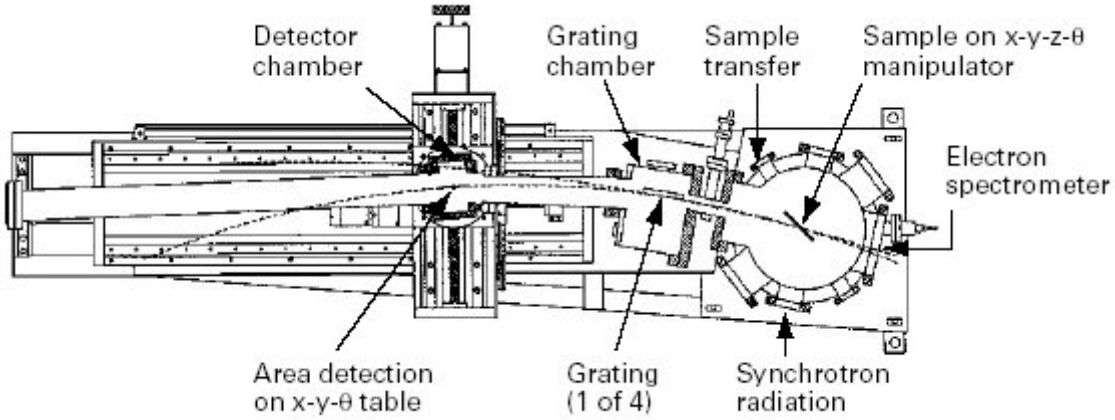

Figure 2.4: The schematic sketch of the soft x-ray fluorescence endstation 8.0.1.[41]

All measurements to date have been performed at Beamline 8.0.1 of the Advanced Light Source in the Lawrence Berkeley National Laboratory[42]. Beamline 8.0 (Figure 2.3) is an undulator beamline, capable of producing photon energies of 70-1200 eV, with an intensity of 10^{12} photons per second at a resolving power ($E/\Delta E$) of 10000. Radiation from the undulator is monochromatized using a grazing incidence, spherical grating monochromator. The water-cooled exit slit is moved so that it and the entrance slit satisfy

Rowland geometry in order to provide optimal focus. A horizontal refocusing mirror is used to compress the beam and refocus the incident radiation on one of four possible end-stations.

Beamline endstation 8.0.1 (Figure 2.4) is a bell jar-type sample chamber with a spectrometer mounted at a right angle to the incident beam. The spectrometer consists of an entrance slit, four interchangeable spherical gratings, and a multi-channel plate detector that are also positioned based on Rowland geometry. We use a 50 μm entrance slit located in the sample chamber approximately 1 cm from the sample. This spectrometer configuration allows energy-dispersive XES spectra to be taken, with a resolution of 150 meV at 100 eV, and 700 meV at 400 eV. In addition, the endstation can be configured to perform both XAS and XES measurements without removing the sample from vacuum.

True absorption of a thin sample would provide the most natural representation of the XAS of the material. However, at 100 eV photon energy, Si_3N_4 has an attenuation length of 5 nm.[43] Because absorption probability increases exponentially with sample thickness, a freestanding sample under observation would have to have a known, uniform thickness much less than 10 nm to expect consistent, quantifiable measurements. In addition to being extremely fragile, samples with such small thickness would provide mostly surface sensitive results. As alternatives, beamline 8.0.1 provides three measurement options for XAS (Figure 2.5).

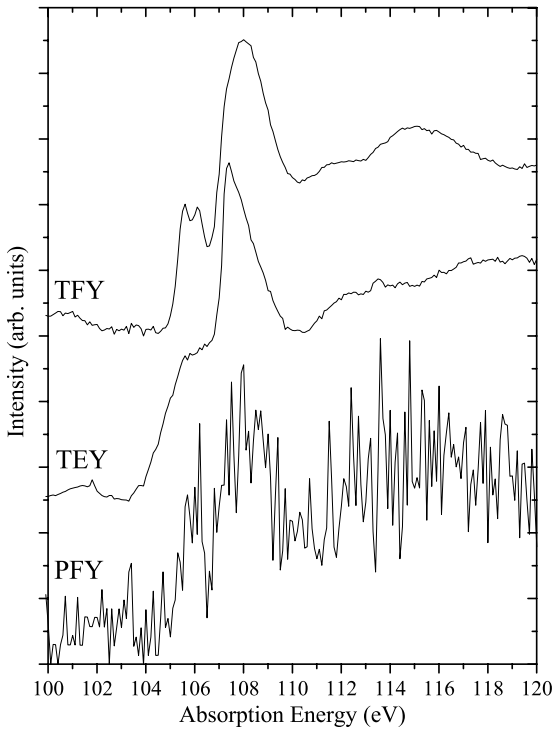

Figure 2.5: Three methods of measuring the $L_{2,3}$ absorption spectra of SiO_2.

The total electron yield (TEY) method involves measuring the current required to neutralize the ionized sample as electrons are removed by the incoming photons. The core hole produced by absorption can be filled by an electron from the occupied states. The electron filling the core hole can give its energy to a neighbouring electron, which is kicked out of the material into the vacuum. The number of electrons being emitted is proportional to the number of electron falling into core holes, which is proportional to the number of core electrons being excited, which is proportional to photon absorption. However, electrons have a much stronger attenuation length than photons, so not all of the electrons can escape. TEY is therefore more surface sensitive than pure photon-in/photon-out methods. This method is also problematic with insulating samples, which show charging affects that skew actual absorption.

Partial fluorescence yield (PFY) involves measuring the emitted radiation accepted by the spectrometer detector. This method therefore provides a measure of the absorption that produces emission within a given energy range. Emitted photons do not suffer from the surface sensitivity associated with TEY. In addition, this method is very useful if one is only interested in electrons emitting within a given energy range. However, since emission is not an efficient process, the spectrometer entrance slit is so small and we are only measuring a limited emission energy range this process requires long measurement times in order to get a measurement with a reasonable amount of noise. The PFY measurement displayed in Figure 2.5 was taken using the same time slices as the TEY and TFY spectra. The results are so noisy that only basic data can be extracted. Longer count time would have produced better results.

Recently, a channeltron was installed in the sample chamber that provides total fluorescent yield (TFY) measurements. This device uses a cascading scintillation process to convert photons (or electrons) into electronic pulses. The head of the channeltron is biased to repel incident electrons, so only photons are measured. Emitted photons do not suffer from shorter attenuation length, which means they produce more bulk-sensitive spectra, and the channeltron measures a wide range of photon energies, increasing intensity and therefore measurement statistics. The emitted photons are still susceptible to self-absorption, which is both a blessing and a curse. Self-absorption causes spectral spreading and reduced intensity as the excitation energy is tuned across additional thresholds (to higher absorption energies). This has a negative impact over the entire energy range of absorption but in the same respect, since the self-absorption is minimal at the absorption onset, TFY increases the intensity and resolution at the absorption onset.

The absorption onset often contains the most interesting features within absorption so this feature is actually quite advantageous.

3 MATERIALS

The four materials discussed in this thesis are α-Si_3N_4, β-Si_3N_4, γ-Si_3N_4, and Si_2N_2O. Some basic properties of the materials are listed in Table 3.1.

Table 3.1: Calculated structural properties and band gaps for the selected materials

Material	α-Si_3N_4[12, 44]	β-Si_3N_4[12, 44]	γ-Si_3N_4[23, 44]	Si_2N_2O[12, 44]
Space Group	$P3_1/c$ (159)	$P6_3/m$ (176)	Fd_3/m (227)	$Cmc2_1$ (36)
Lattice Constants (Å)	a = 7.792 c = 5.614	a = 7.622 c = 2.910	a = 7.837	a = 9.008 b = 5.397 c = 4.904
Si coordination	4	4	4, 6	4
N coordination	3	3	4	3
Average NN Length (Å)	1.735	1.740	1.824 (4) 1.889 (6)	1.721 (Si-N) 1.624 (Si-O)
E_{Gap} minimum (eV)	4.63	4.96	3.45	5.20
E_{Gap} direct at Γ (eV)	4.67	5.25	3.45	5.20

3.1 α-Si_3N_4/β-Si_3N_4

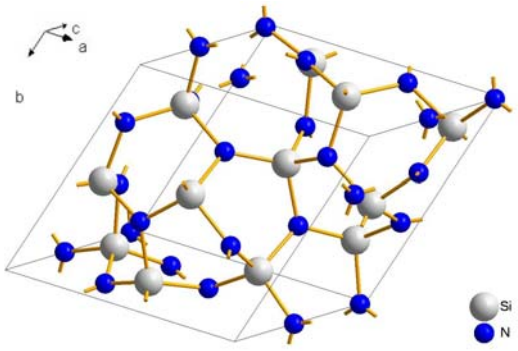

Figure 3.1: Crystal structure of α-Si_3N_4[45]

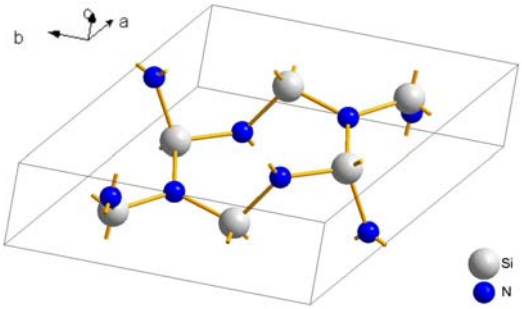

Figure 3.2: Crystal structure of β-Si_3N_4[46]

α-Si_3N_4 and β-Si_3N_4 are the lowest energy phases of silicon nitride, and until recently have been considered the only phases of Si_3N_4. They are very similar in structure and function, so they are often lumped together when discussing "nitrides" in literature. α-Si_3N_4 (Figure 3.1) is characterized by a trigonal lattice structure. It contains Si atoms that are each connected to four N atoms to form a tetrahedron, and N atoms surrounded by three Si atoms in a planar arrangement (trigonal). The entire structure is planar with stacking pattern ABCDABCD… β-Si_3N_4 (Figure 3.2) is characterized by a hexagonal lattice structure. It also contains Si atoms that are surrounded by four N atoms in a tetrahedral coordination, and N atoms surrounded by three Si atoms in a trigonal arrangement. The overall structure is planar, with stacking pattern ABAB…

Even in large crystal grain sizes, electronic properties of α-Si_3N_4 and β-Si_3N_4 resemble amorphous Si_3N_4. The resemblance of the materials is so good that there is a consensus that amorphous Si_3N_4 naturally forms a mixture of polycrystalline Si_3N_4 phases when pressed. This is most likely due to the strong localization of the silicon sites, which will be discussed further in Section 4.1.

Mechanically, both of these materials are very hard and resistant to oxidation. These two factors make Si_3N_4 ceramics useful for cutting tools and other industrial applications. Although each crystal itself is very hard, the overall ceramics containing α and β-Si_3N_4 are relatively brittle. This has been attributed to the crystal grain interface with the ceramics glassy region. Crystal growth research has overcome this problem by creating β-Si_3N_4 "whiskers."[47] These elongated crystal grains along with an overall bimodal grain size make β-Si_3N_4 much stronger. However, producing the same structure with α-Si_3N_4 has proven more difficult.

Crystal growth researchers have been experimenting with different ways of further increasing the hardness and resistance to intense heat of these materials. It has been found that the introduction of aluminium and oxygen into the ceramics can produce such results. These new class of ceramics are known as SiAlON ceramics. Much of the literature on crystal growth of silicon ceramics is currently focussed on such SiAlONs.

Electronically, α-Si_3N_4 and β-Si_3N_4 are considered insulators. They have wide indirect band gaps (4.67 and 4.96 eV respectively [12, 44]) and are used as both insulators and protective layers in integrated circuits. The most common method of applying Si_3N_4 to a silicon wafer in integrated circuits is chemical vapour deposition (CVD), which creates a generally amorphous thin film of material. When used as an insulator, nitrides can produce a quantum well used to trap electrons, or increase switching voltages. Such metal-nitride-oxide-semiconductor (MNOS) devices are common in non-volatile memory and certain solar cells.[48] When used as a protective layer, Si_3N_4 can be found in FinFET applications [49] or used as a diffusion barrier.

In this study, a polycrystalline sample of α-Si_3N_4 is used. It was measured in both pressed and powered forms, with identical results. The sample is yellow-grey in colour and translucent. For β-Si_3N_4 a single crystal sample was used. The sample was transparent, and measured approximately 2 mm x 2 mm x 0.1 mm.

3.2 γ-Si_3N_4

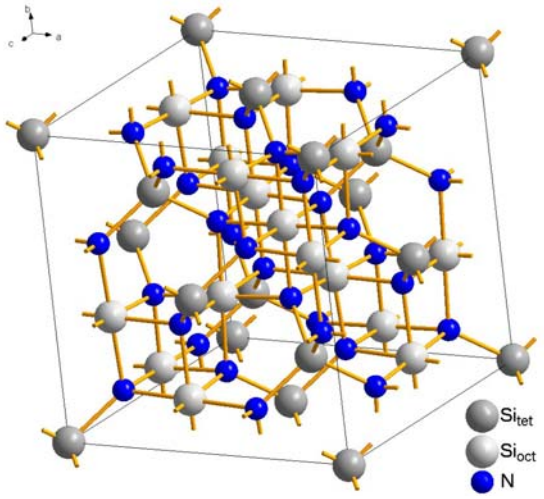

Figure 3.3: Crystal structure of γ-Si_3N_4[21]

Originally synthesized by Zerr et al[21] in 1999, γ-Si_3N_4 is the highest-energy phase of Si_3N_4 requiring an environment of 13 GPa and 1800 K to form. This phase is harder than the previous two phases and, when it was first synthesized, was second only to diamond as the hardest known material. In addition to being very hard, this nitrogen ceramic is extremely resistant to oxidation. These two properties alone make γ-Si_3N_4 valuable for mechanical devices such as cutting blades.

γ-Si_3N_4 has a face-centred cubic spinel structure (Figure 3.3) in which nitrogen atoms surround Si atoms in two different arrangements. Six nitrogen atoms surround octahedral silicon sites while four surround tetrahedral sites. The octahedrally bonded silicon is unique to γ-Si_3N_4. In fact, although observed frequently in oxide ceramics, γ-Si_3N_4 was the first nitride ceramic where this six-fold arrangement of N anions was observed. This discovery prompted a flurry of research into materials that could benefit from a spinel

structure, including spinel-phase C_3N_4, which is predicted to be harder than diamond, but has proven to be difficult to synthesize in a pure form.[50]

According to ab-initio calculations, γ-Si_3N_4 is a wide-gap semiconductor, with a direct band gap of 3.45 eV.[23] Ultraviolet emission from this band gap would be useful for light emitting devices, as it can either be used directly or changed to visible light using phosphors. Likewise, semiconductor-based power systems that are based on wide-gap semiconductors benefit from increased efficiency, reliability, and temperature tolerance. However, experimental verification of this band gap has not been published, which is a straightforward process using SXS.

In this study, a polycrystalline sample of γ-Si_3N_4 is used. The γ-Si_3N_4 powder was synthesized by Toshimori Sekine from β-Si_3N_4 by the shock compression method[51] and purified by a hot hydrofluoric acid solution.[52] The powder has been characterized using x-ray diffraction, Differential Thermal Analysis[53] and ^{29}Si magic-angle-spinning NMR.[28] The oxygen content of the purified γ-Si_3N_4 has been determined to be 2.0 wt% by a high temperature combustion method in the LECO Co. furnace. Therefore, the γ-Si_3N_4 powder is considered to consist of pure nitride spinel phase. The sample is known to have a grain size of 10-50 nm.

3.3 Si_2N_2O

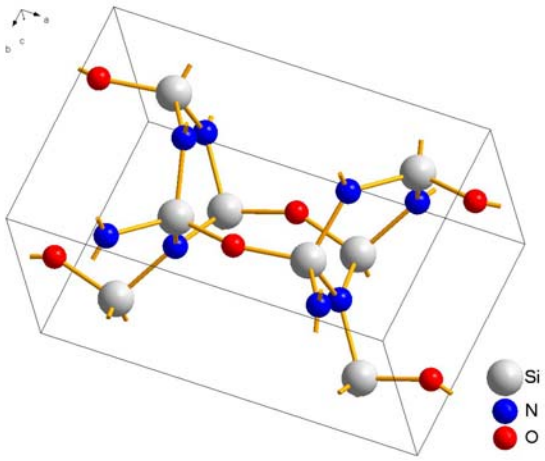

Figure 3.4: Crystal structure of Si_2N_2O[54]

Although Si_2N_2O has been around for many years, its uses have been limited until very recently. Si_2N_2O is characterized by an orthorhombic lattice structure. The overall structure is a network of sheets of Si_2N_2 interconnected by O atoms. N atoms are still surrounded by three Si atoms in a trigonal structure while Si retains its tetrahedral bonds with one of the N atoms being replaced by O. The unit cell for Si_2N_2O is pictured in Figure 3.4.

The reason Si_2N_2O has not been widely used until recently is its very wide band gap. At 5.20 eV, it is very much an insulator. It is not as hard as α-Si_3N_4 or β-Si_3N_4, so has limited mechanical applications. However, Si_2N_2O has been proposed for use in integrated optical communications devices.[31] By bombarding a quartz substrate with nitrogen, Si_2N_2O can be integrated into the material. By adjusting the amount of N introduced into the material, the index of refraction of the material can be "tuned"

creating a planar wave-guide. This technique has been used to produce polarization controllers, couplers, filters and switches.

In the present study, a polycrystalline pressed and powdered sample of Si_2N_2O was used. It is white-grey in appearance and exhibits no glossy finish.

4 RESULTS/DISCUSSION

4.1 Si $L_{2,3}$ Absorption

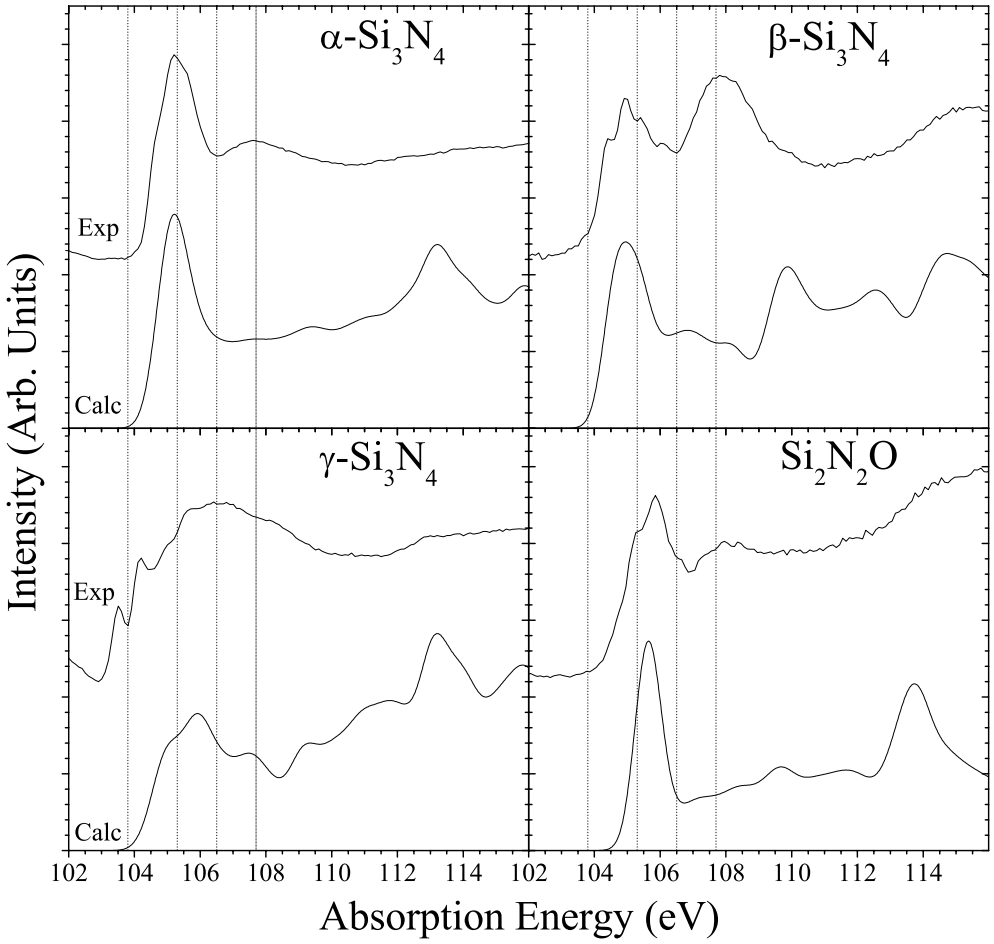

Figure 4.1: Measured Si $L_{2,3}$ x-ray absorption spectra with corresponding calculated spectra.

The most common and most published spectra available for these materials are the Si $L_{2,3}$ spectra (both absorption and emission). α-Si_3N_4 and β-Si_3N_4 absorption spectra have been well published[14, 20, 29, 32, 55-59] while both γ-Si_3N_4 [29, 60] and Si_2N_2O [61] have only a few published results. Figure 4.1 shows our XAS spectra for the four materials, along with the associated calculated XANES spectrum. Vertical lines placed on the

spectra indicate areas of interest. Discounting the ratio of peaks, three of the experimental spectra: α-Si_3N_4, β-Si_3N_4, and Si_2N_2O have very similar spectral features in terms of energy. This emphasizes the importance of local coordination of Si in these types of materials, which is much stronger than the influence of alternate elements, as is the case with Si_2N_2O, or overall crystal structure changes, as is the case with α-Si_3N_4/β-Si_3N_4. γ-Si_3N_4 is the only material to show a substantial spectral deviation. It is also the only material to exhibit a change in the local coordination of Si atoms with the introduction of octahedral Si. By comparing the three similar experimental spectra to that of γ-Si_3N_4, it appears that the inclusion of octahedral Si causes a superposition of two spectra: Si_{tet} and Si_{oct}. This conclusion seems valid, again considering the highly localized nature of Si $L_{2,3}$ absorption spectra.

Since the experimental spectra are similar, in order to discuss the features of each spectrum we need only discuss the general shape of all of the experimental spectra.

The vertical line at 105.3 eV indicates an area of the spectra due to the onset of the conduction band DOS. Sharp peaks characterize the onset, which are not found in the onset of crystalline Si.[56] These peaks have been attributed to localization of states in the conduction band. The localization effect increases the lifetime of electrons that are excited to these states, therefore reducing lifetime broadening and producing sharp peaks. These localization effects have been documented for SiO_2, as well as other ceramics not containing Si.[62] O'Brien et al show that these states are indeed due to conduction band states by measuring their emission. Since these states are nearest the Fermi edge, they can be populated thermally. Since they are populated, there is a chance for emission to occur. It is interesting to note the similarities of the peak structure within this energy range for

each of the materials. All three materials exhibit a 4-peak structure, with similar peak ratios and relative energy positions. The only observable change is the overall location of the peaks, which is shifted to lower energy in β-Si_3N_4 and higher energy in Si_2N_2O compared to α-Si_3N_4. The peak resolvability also changes for each spectrum. This resolvability or "sharpness" is most likely due to manufacturing processes of the materials measured as well as measurement factors rather than effects of the materials themselves.

After the localized onset, the spectra exhibit a delocalized band-like $L_{2,3}$ onset. This absorption feature is broad compared to localized onset discussed earlier, which is due to the short lifetime of electrons in these delocalized states. There is very little to resolve from this peak, other than it's location and relative intensity. When comparing to the calculated spectra, it should be noted that this area is not very well represented. This may be due to the inability of the calculations to account for the localization of the near-edge states or it may simply be "washed out" due to the constant broadening factor used in XANES.

In a similar respect, the onset of L_1 absorption can be seen above 112 eV. This peak is very broad, and similar in nature to the $L_{2,3}$ band onset. When comparing the measured and calculated spectra, each of the calculated XANES show a peak that corresponds in energy to the L_1 onset, although it appears that the calculations over-estimate its influence on the absorption spectra.

The Si $L_{2,3}$ absorption spectrum of γ-Si_3N_4 is different from the absorption spectra of the other materials, which is attributed to the presence of octahedrally coordinated Si. Si_{oct}

produces a different absorption spectrum than Si_{tet}. Since γ-Si_3N_4 contains both tetrahedral coordinated Si and octahedral coordinated Si, the absorption spectrum is a superposition of absorption from these two non-equivalent sites. The peak appearing under the vertical line at 106.5 eV in the γ-Si_3N_4 absorption spectrum is the $L_{2,3}$ onset for Si_{oct}. This peak overpowers at least two of the four peaks of the localized tetrahedral onset since there are twice as many octahedral Si sites as tetrahedral. Si_{oct} does not appear to exhibit the same localization features found in Si_{tet}. The two sharp onset peaks under the vertical line located at 103.8 eV are also present only in γ-Si_3N_4. These peaks are highly localized, but they are not attributed to localization of the conduction band as with the Si_{tet} onset. Instead, these peaks are attributed to newly created excitonic states within the band gap. Excitonic states are electron-hole pair states that are created by coulombic interaction. When an electron is excited from a core state, it is excited to a state localized around the atomic site. Since the electron and the newly created core hole both represent charged particles (or virtual charged particles), they exhibit coulombic interaction. This interaction can create electronic states that would otherwise not exist in the system, including states that exist within the band gap.

4.2 N K Absorption

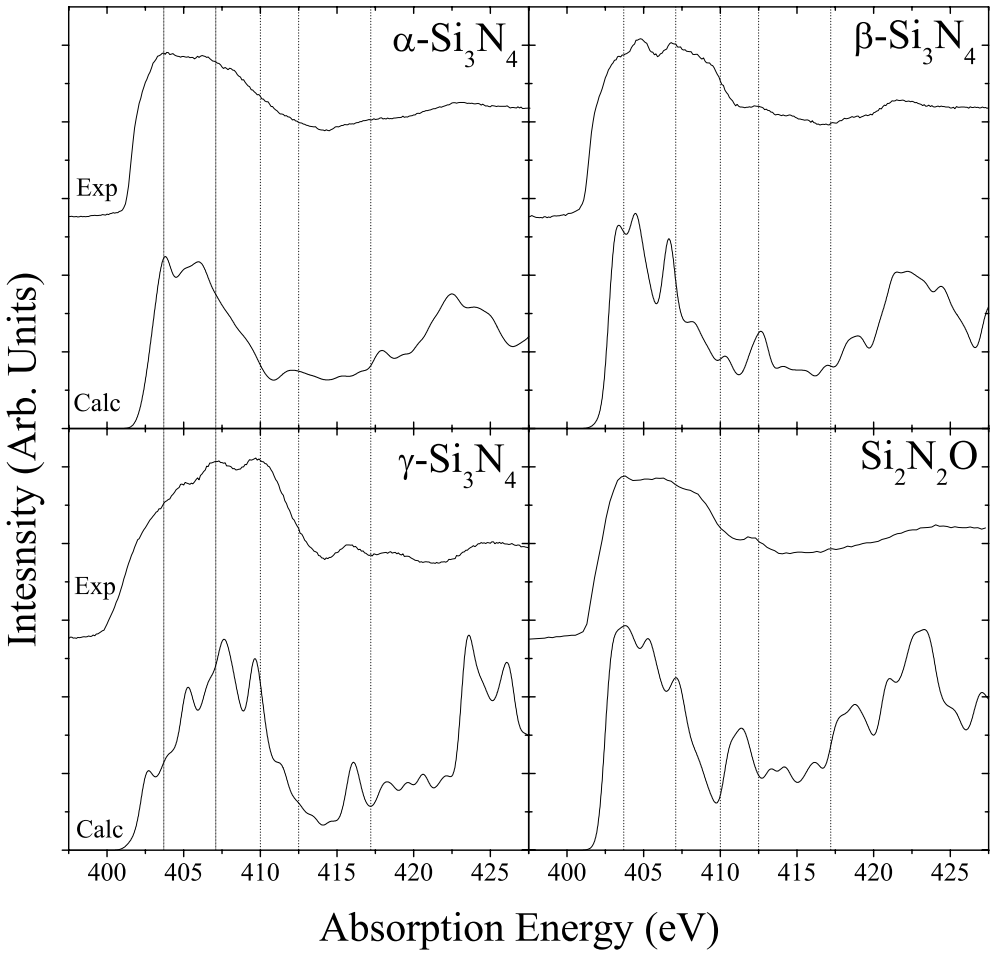

Figure 4.2: Measured N K x-ray absorption spectra with corresponding calculated spectra.

The N K absorption spectra as well as calculated XANES are shown in Figure 4.2. Vertical lines placed on the spectra indicate areas of interest. A literature search revealed few previously documented N K spectra of silicon nitride, and only of amorphous samples created by bombarding Si with N atoms. [63, 64] These spectra therefore represent some of the first N K spectra of these materials. The gradual onset of the γ-Si_3N_4 absorption spectrum at ~402 eV is lower than the other three materials. This early

onset causes a reduced band gap that is consistent with band gap values discussed in Section 4.7. The N K onset for the other three materials is much sharper, and comes to a peak located near 403.7 eV. All of the spectra exhibit a strong peak under the vertical line located at 407.1 eV except β-Si_3N_4, where it can be resolved into two separate peaks. This is corroborated with the calculated spectra, and is a result of the band structure in that energy range. It is interesting to note that this same splitting appears in the calculated XANES for γ-Si_3N_4, even though it does not appear in the measured spectrum. There is a shoulder located near 410 eV on all of the spectra but γ-Si_3N_4, where it is yet another peak. The location of this feature is reproduced in the calculated XANES, however the intensity is not. The extended absorption spectra exhibits additional small peaks near 412.5 eV and 417.2 eV. These features are remarkably well reproduced in the calculated spectra. Finally, there is a bump in each spectrum located above 420 eV, which coincides with the L_1 absorption edge for the Si spectrum.

Unlike Si, N spectra differ significantly for different materials. However, the fact that the spectra differ for each material is not as interesting as the existence of observable fine-detail superimposed on the onset. Nitrogen absorption spectra have been used in the past to determine nitrogen content of amorphous SiN_x films.[63, 64] It turns out that an excitonic peak appears in the spectrum that increases as a function of nitrogen content. The important part to note about these studies is the shape of the nitrogen spectra. The amorphous SiN_x spectra have one large onset with no observable variation, while the nitrogen spectra shown in Figure 4.2 have observable features within the same energy range. This means that electronic states surrounding the N atoms must be influenced by the crystal structure as a whole.

The fact that the N spectra have more variation for a crystal then for an amorphous sample is somewhat counter-intuitive. When atoms arrange in a crystal, the outer band electrons switch from localized atomic orbitals to delocalized band states. This delocalisation process increases the density of states possible in a given energy range, thereby decreasing the lifetime of electrons in any given state and increasing the broadening factor. The absorption spectra for a given element should become more "washed out" in a crystalline material then an amorphous material, which is not the case for the nitrogen K edge. Instead, the N K edge appears to be sensitive to the long-range order associated with crystal structures, which can be exploited to determine the overall structure of an unknown material.

4.3 O K Absorption

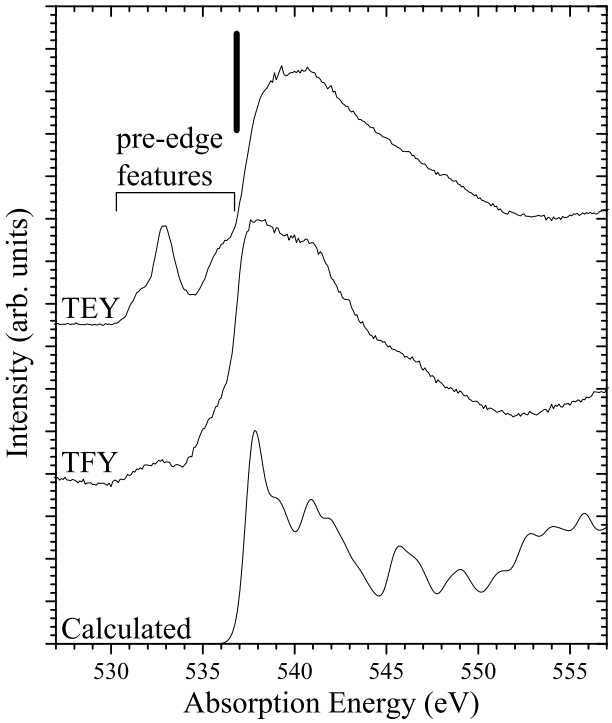

Figure 4.3: Measured O K x-ray absorption spectra with corresponding calculated spectra.

The oxygen K edge absorption spectra are shown in Figure 4.3. Both TEY and TFY measurement methods are included, along with the calculated XANES spectrum. O K absorption spectra of Si_2N_2O have only recently been documented, and those spectra were performed on only amorphous thin film samples. These spectra therefore represent the first O K emission spectra of polycrystalline Si_2N_2O. The spectra exhibit three pre-edge features that appear between 531 eV and 536 eV, a sharp onset at ~536 eV, followed by a gradual peak at ~540 eV with limited features. The two measured spectra agree with the calculated XANES spectrum (bottom) excluding the pre-edge features.

The short vertical line at 536.4 eV represents the calculated onset of the conduction band, which was derived by aligning the O K emission spectrum to the calculated LPDOS spectrum and extending it beyond the Fermi energy to the onset of the conduction band. While this method does not take into account any spectral shifting due to the presence of the core hole, it gives a good approximation of the location of the calculated conduction band onset. It is clear that the pre-edge features exist entirely within the band gap; however, it is not clear whether the pre-edge features are due to impurities in the apparatus or actual material properties that are not modelled in the calculated XANES. In order to clarify this, we compare our spectra to those of α-SiO_2 and amorphous Si_2N_2O thin films measured by McGuinness et al.[32] The O K absorption spectra for these two materials are similar to our acquired spectrum of poly-crystalline Si_2N_2O, excluding the appearance of the pre-edge features. This means that either the pre-edge features are impurity based, or crystalline Si_2N_2O exhibits properties that no other Si-O ceramic exhibits, the later of which is very unlikely.

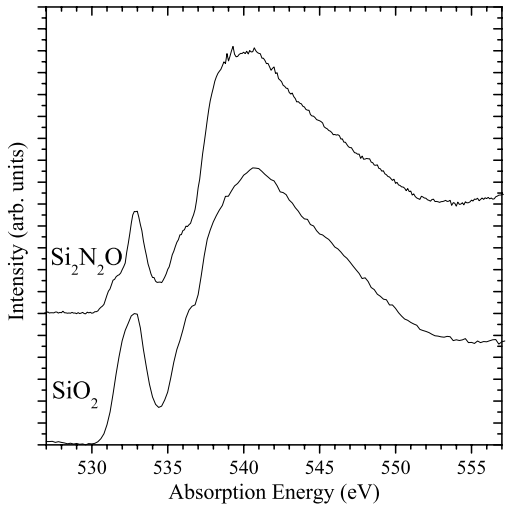

Figure 4.4: Total electron yield O K absorption spectra for Si_2N_2O and SiO_2.

The O K absorption spectra are presented along with the same spectra taken for crystalline SiO_2 in Figure 4.4. The two spectra are nearly identical and any difference is attributed to the same impurities or instrumental anomalies that cause the pre-edge features. The similarities of these results, as well as those of McGuinness et al shows that unlike N 2p LPDOS, O 2p LPDOS does not change dramatically in a crystalline form compared to an amorphous material, nor does it change with the structure of a material when compared with absorption spectrum of SiO_2. We conclude that O K edge absorption does not provide any new insight into the material.

4.4 Si $L_{2,3}$ Emission

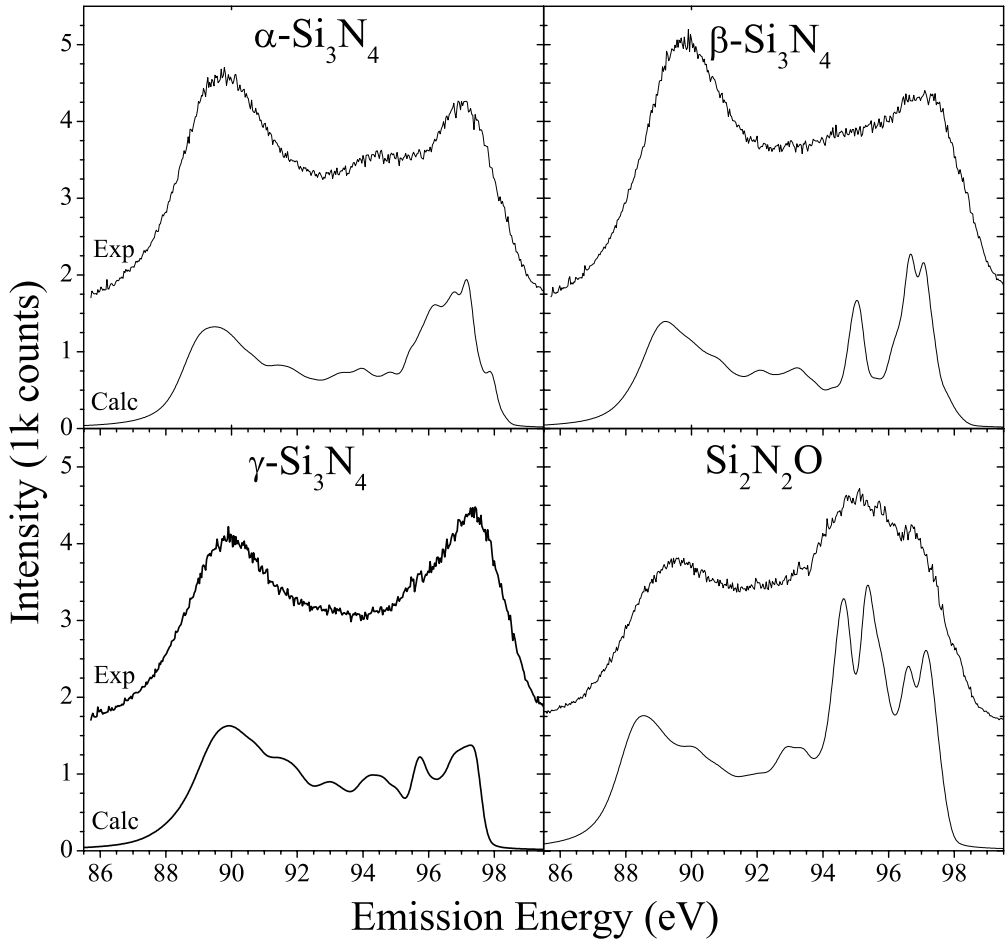

Figure 4.5: Measured Si $L_{2,3}$ x-ray emission spectra with corresponding calculated spectra.

Figure 4.5 shows the Si $L_{2,3}$ emission spectra for the four materials along with the corresponding calculated emission spectra. The calculated emission spectra were derived from the LPDOS for s and d orbitals, and were broadened as discussed in Section 2.3. As with Si absorption, Si $L_{2,3}$ emission spectra are very similar for each material. In order to get an idea about the structure of each emission spectrum, we need only examine the details of the emission spectrum for one.

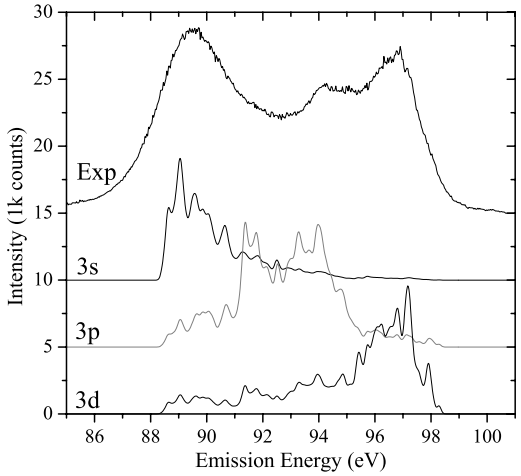

Figure 4.6: Measured Si $L_{2,3}$ emission spectrum with Si orbital symmetry breakdown for α-Si_3N_4 LPDOS below the Fermi level.

Figure 4.6 shows a breakdown of the measured Si $L_{2,3}$ emission spectrum of α-Si_3N_4 along with the orbital symmetry breakdown for those symmetries that contribute to the Si LPDOS within that energy range. The Si $L_{2,3}$ emission spectra can be broken into two sections:

- 85-95 eV bonding states with sp^3 symmetry
- 95-100 eV non-bonding states of d symmetry

The assignment of bonding versus non-bonding states derives from the classical description of the arrangement of atomic states within the structure. Bonding states create classically attractive forces, while non-bonding states create classically repulsive forces. The assignment of bonding/non-bonding has been analyzed by Liu and Cohen by mapping of valence band states in real space.[65]

The Si sp^3 bonding states in the energy range 85-95 eV are caused by the valence 3s and 3p symmetries hybridizing to form tetrahedral coordinated orbitals that bond with

neighbouring N p orbitals. In an LPDOS calculation, hybridization is shown as overlapping LPDOS features. Between 85 and 95 eV, s and p LPDOS are the major contributing factors to the density of states and overlapping features are evident, which agrees with the classical description. Since emission must follow dipole selection rules, only those portions of the LPDOS that correspond to s symmetry appear in the $L_{2,3}$ emission.

The energy range 95-100 eV is considered non-bonding Si d states. There has been some controversy over whether the Si d states contribute to the overall structure of the material through non-bonding interaction with N p states through a so called p-dπ interaction.[12, 13, 65, 66] Liu and Cohen[65] have shown that there is no overlap of Si and N states in this energy range, and concludes that there is therefore no interaction between these states. Our current calculation shows a very strong Si d component in the emission spectrum at this energy and indicates a strong interaction between Si d and N p states within this energy range. This non-bonding interaction is discussed in more detail in Section 4.5.

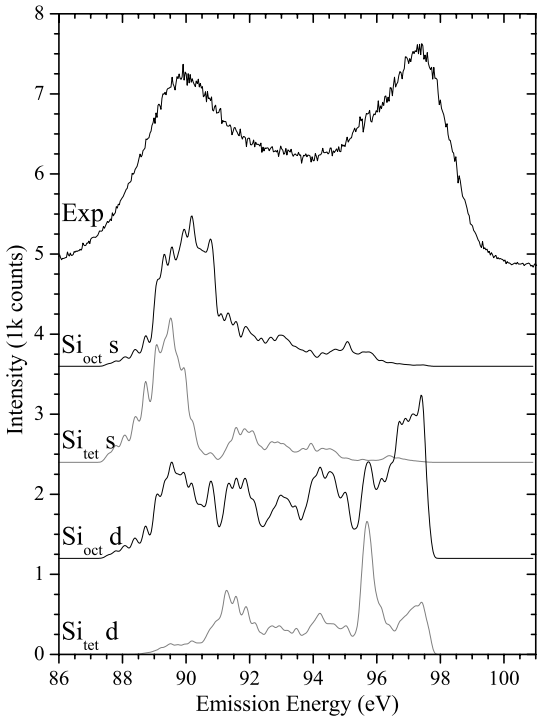

Figure 4.7: Si $L_{2,3}$ emission spectrum and orbital/site symmetry LPDOS for γ-Si_3N_4 Si s and d states below the Fermi level.

Octahedral silicon introduced in γ-Si_3N_4 does not follow the classical sp^3 tetrahedral hybridized orbitals and we can therefore not expect a simple set of hybridized s and p symmetries in the 85-95 eV bonding region. In fact, the octahedral coordination is identical to how a completely filled d valence shell would bond with neighbouring atoms. Therefore, a first approximation would suggest that Si_{oct} would be caused by a completely filled d shell. To verify this the breakdown of s and d LPDOS for both octahedral and tetrahedral Si is shown in Figure 4.7. Contrary to the first approximation, the LPDOS for s symmetries between Si_{tet} and Si_{oct} changes very little, as does the LPDOS for p symmetries (not shown). The major change for Si_{oct} is only with the influence of the Si d states in the bonding region. The d symmetric states have a strong influence in the 88-91 eV energy range for Si_{oct}, but they are near zero for Si_{tet}. Instead of rearranging the valence band to consist of only d states, electrons with d symmetry act to

stabilize the already sp hybridized bonding arrangement for Si, creating what could classically be called an sp^3d^1 hybridized orbital. Meanwhile, the non-bonding region remains unaffected.

For Si_2N_2O, the influence of oxygen on Si becomes apparent. The non-bonding region of this spectrum is extended to 94-100 eV to accommodate a strong peak due to interaction of Si 3d states with O 2p states. Like the p-dπ interaction between Si and N, this interaction is thought to cause changes in the overall structure of the material, and is discussed in more detail in Section 4.6.

4.5 N K Emission

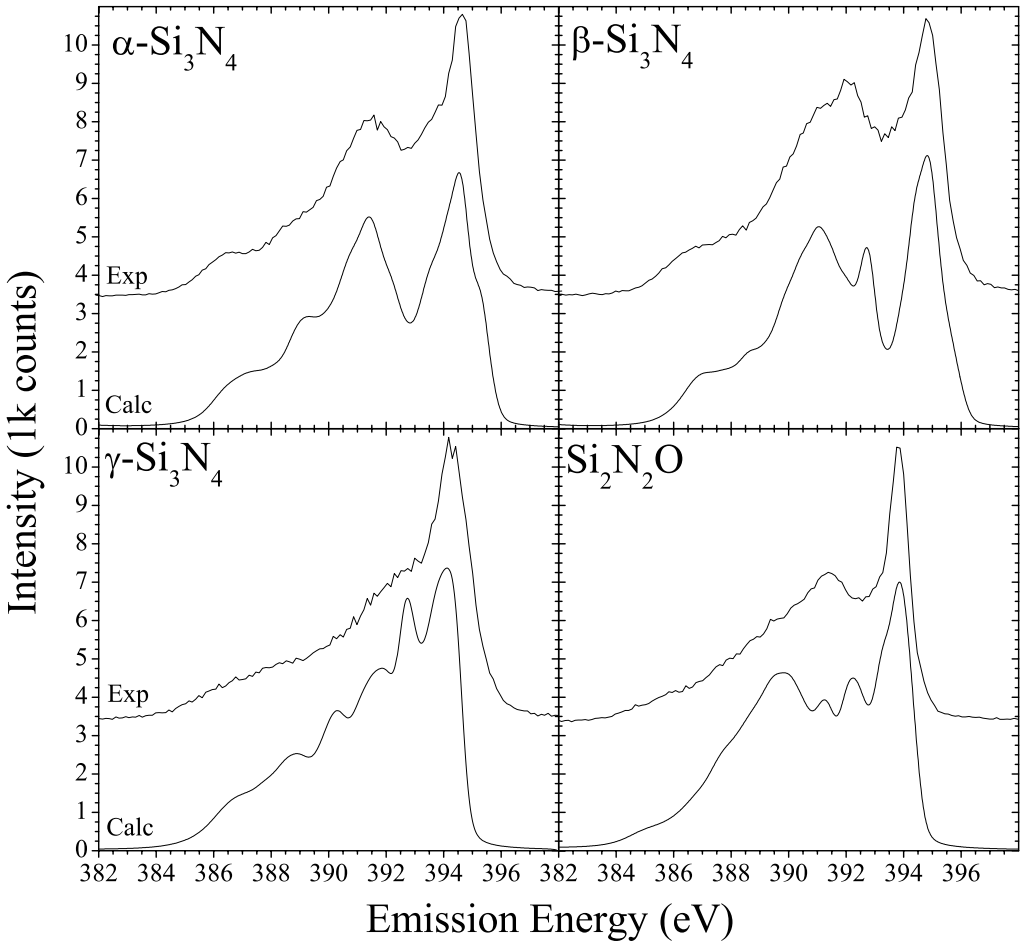

Figure 4.8: Measured N K x-ray emission spectra with corresponding calculated spectra.

The N K emission spectra of the materials are shown in Figure 4.8, along with calculated spectra. The calculated spectra are produced by taking the LPDOS for N p symmetries and broadening them using methods described in Section 2.3. All of the spectra show a strong peak at the high-energy onset (~394 eV), with a more distinct and variable structure throughout the remaining spectra. Previously published results [12, 13, 66] of α and β-Si_3N_4 state that the high-energy peaks arise from lone-pair non-bonding orbitals in

the p_y plane, while the remaining structure is a result of $p_{x,y}$ states bonded with neighbouring Si sp^3 orbitals. These conclusions are corroborated by Liu and Cohen[65] by examining the electronic DOS of states in these energy ranges. Previously published N K emission spectra of γ-Si_3N_4 and Si_2N_2O could not be found.

Instead of the traditional four-fold $p_{x,y}$ planar arrangement of bonding orbitals, α-Si_3N_4, β-Si_3N_4 and Si_2N_2O nitrogen bonding takes a planar trigonal structure, containing only a three-fold connection to neighbouring atoms. γ-Si_3N_4 goes one step further by extending the N structure to a four-fold tetrahedral symmetry. Researchers have put forth many theories as to why N warps into this non-traditional structure.

The first and most straightforward solution would be sp^2/sp^3 hybridization in the $p_{x,y}$ bonding states. Hybridized sp^2 orbitals arrange in a trigonal symmetry, and sp^3 orbitals arrange in a tetrahedral symmetry, which would account for the change in geometry. Hybridized states cause overlapped LPDOS with corresponding features, so by examining both s and p symmetries in the valence band we can determine if hybridization exists. Figure 4.9 shows an extended spectrum for N K emission of α-Si_3N_4 as well as the breakdown of the LPDOS in the same energy range.

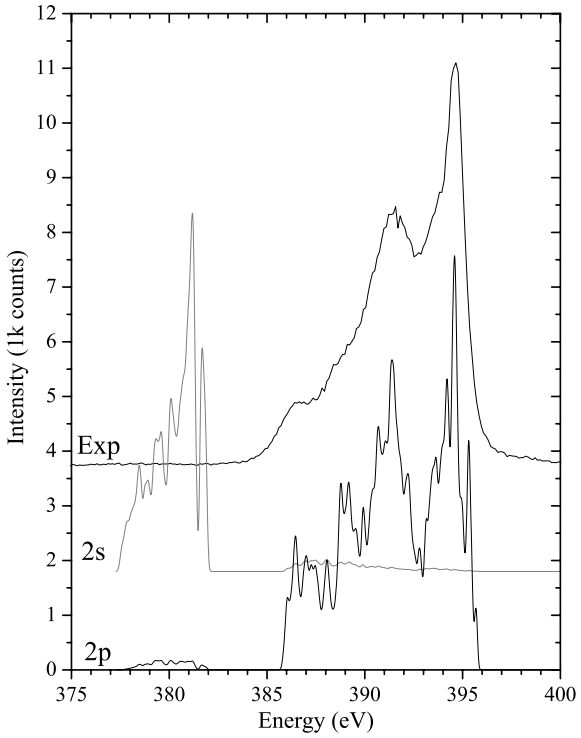

Figure 4.9: N K emission spectrum of β-Si_3N_4 with LPDOS breakdown for N states below the Fermi level.

From Figure 4.9, there is little doubt as to the origin of the valence band. The K emission matches p states quite well, and there is virtually no emission from the band containing s states. In fact, there is a ~4 eV gap between states with s symmetry and p symmetry. This is a good indication that there is no sp hybridization occurring. While L emission would complete the argument (showing the s symmetric states, but not the p states), this comparison gives a good indication that the calculations are correct.

The second theory involves a p-dπ interaction between N and Si. This theory states that N p orbitals interact with Si d orbitals in a π interaction. A π interaction is one where the electron densities of the two interacting atoms do not overlap. In order to illustrate the possibilities of this theory, we must look at a breakdown of the Si and N emission on a corresponding energy scale.

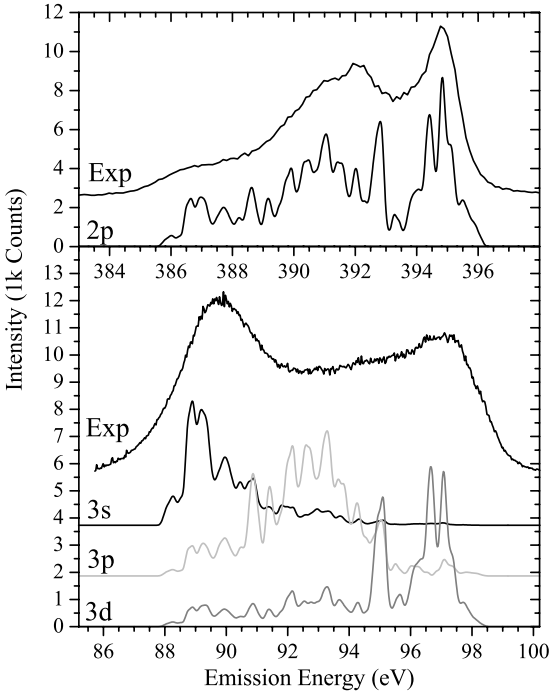

Figure 4.10: Measured x-ray emission spectra with orbital symmetry breakdown of LPDOS of Si and N in β-Si_3N_4.

Figure 4.10 shows the orbital symmetry breakdown for both Si and N sites. The energy scales have been adjusted so that the onset of the valence bands line up vertically. Just like hybridization of orbitals in a single atom, orbital symmetries that interact between sites will appear as overlapped LPDOS with similar features. We know from the discussion of Si emission (Section 4.4) that Si states with sp^3 symmetry bond with N p states below 96 eV. Therefore, when comparing calculated LPDOS for N p symmetry with Si 3s and 3p symmetry, we should observe overlapping features, which is indeed the case. Likewise, if there is an interaction between N p and Si d states, there should be overlapping spectral features in the corresponding energy range (> 95 eV for Si, and > 393 eV for N), which is also the case. Therefore, we can conclude that p-dπ interaction can explain some the change in configuration of N.

A third theory states that nearest-neighbour N atoms interact to deform the N structure. The high-energy onset peak in each N spectrum represents a high density of non-bonded orbitals. It is possible that these electrons interact over a long range to neighbouring N sites much like the p-dπ interaction between Si and N. However, unlike Si and N interaction, it is very difficult to extract information about individual N sites within the material in order to verify this theory. The most likely conclusion is that both p-dπ interaction and nearest neighbour interaction cause the deformed N structure.

4.6 O K Emission

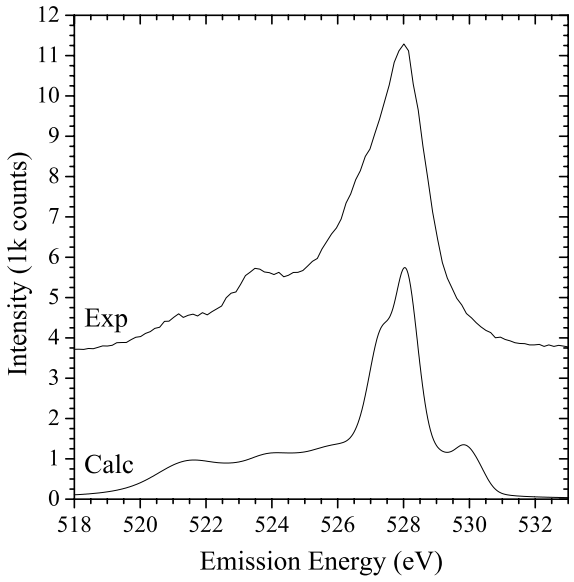

Figure 4.11: Measured O K x-ray emission spectra with corresponding calculated spectra.

The O K edge emission spectrum for Si_2N_2O is shown in Figure 4.11. It has a very simple structure similar to that of nitrogen. Like nitrogen, the majority of states within this energy range exhibit 2p character. The O K emission therefore gives a good indication of not only the partial density of states surrounding the oxygen sites, but also the total

density of states of the oxygen valence band. Other groups have measured O K emission of Si_2N_2O in amorphous thin-films and provided very similar results.[32]

The O K emission spectrum is also very similar to that of α-SiO_2 presented by McGuinness et al,[32] which is to be expected since the electronic environment of the O in both materials are very similar. However, the similarities between α-SiO_2, amorphous Si_2N_2O and polycrystalline Si_2N_2O are so strong that very few conclusions can be drawn from their comparison alone.

By comparing the O K emission spectrum to the calculated spectra, we can see good agreement in all areas, save the location of the high-energy onset. In the calculated spectrum, there is an extra feature at ~539 eV that results from hybridization of O and N electrons. The measured emission spectrum does not exhibit this same feature. It is concluded that the O and N electrons do not hybridize, causing a different valence band onset for each site. It is important to note that the O valence band has a lower onset energy than the N valence band and therefore the band gap for O is also larger than that of N or Si.

Like nitrogen, oxygen bonding in Si_2N_2O has a deformed structure. Normally oxygen atomic orbitals arrange to form bonds with two neighbouring atoms with a bond angle of ~90°. In Si_2N_2O that bond angle is stretched to nearly 180°. This increase in bond angle is found in many Si-O ceramics and is caused by the same interactions that cause the change in bonding arrangement in nitrogen.

4.7 Non-equivalent Sites

The unit cell of a material often contains multiple atoms of the same element. These atoms may have a different electronic density surrounding them and therefore different electronic properties. The study of non-equivalent sites involves isolating properties of the unique electronic structure of these non-equivalent atoms.

It is well known that x-ray spectroscopy is sensitive to specific elements. However, SXS is also a localized process. An electron transition takes place in the proximity of one atomic site and does not cause significant perturbation to neighbouring sites. The unique LPDOS of the non-equivalent sites therefore provide unique, overlapping soft x-ray spectra. The goal of non-equivalent site research is to verify and quite possibly extract the unique spectra associated with these unique LPDOS.

This type of research is relatively new to the field of SXS and therefore methods of analyzing non-equivalent sites are still in development.[67-69] With Si atoms in both tetrahedral and octahedral sites, γ-Si_3N_4 provides a material that is relatively easy to model and has very distinct non-equivalent sites. It is therefore an optimal material for developing methods to analyze non-equivalent sites. The goal is to extract the information that is unique to each non-equivalent Si site based on electronic structure, and to perform this using a sample with polycrystalline grain structure randomly oriented in space.

Currently, this is accomplished through the combined use of calculations and experiment. Calculated XANES spectra can be broken down based on each of the non-equivalent sites. Since these spectra represent the probability of exciting an atom in each of the non-

equivalent sites independently, they also represent the probability of creating a core hole in that same site. The resulting emission spectrum will exhibit the LPDOS of each of the non-equivalent sites combined, with the ratio based on that excitation probability. This method is very similar to one used by Guo et al on $La_{2-x}Sr_xCuO_4$.[70]

The contribution of incident photons to produce core holes in each non-equivalent site is not only based on the ratio of LPDOS, but also on the degree of lifetime broadening and proximity to resonant peaks. These factors make the proportion of emission spectra from each non-equivalent site not exactly known, and therefore make the emission difficult to determine. In order to extract XES from each site, they must be excited with a high degree of exclusivity. The challenge of this technique is providing this sufficient degree of exclusivity. Resonant excitation at well-defined features in the absorption spectra is used to increase the ratio of core holes produced in each non-equivalent site. For γ-Si_3N_4, this is accomplished by exploiting the excitonic peaks. Excitonic states produce a core hole by exciting an electron to a coupled electron-hole state, giving rise to additional electronic states in the (otherwise forbidden) band gap. These sharp spectral features are localized to each non-equivalent site and therefore provide a high degree of exclusivity.

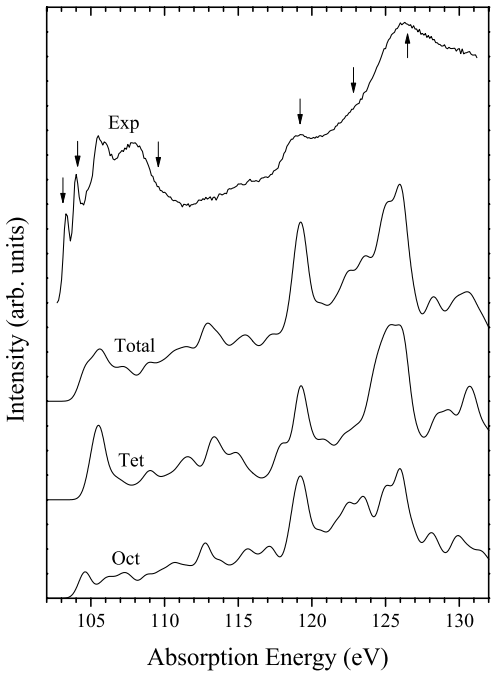

Figure 4.12: Measured Si $L_{2,3}$ absorption with calculated, site-selective XANES.

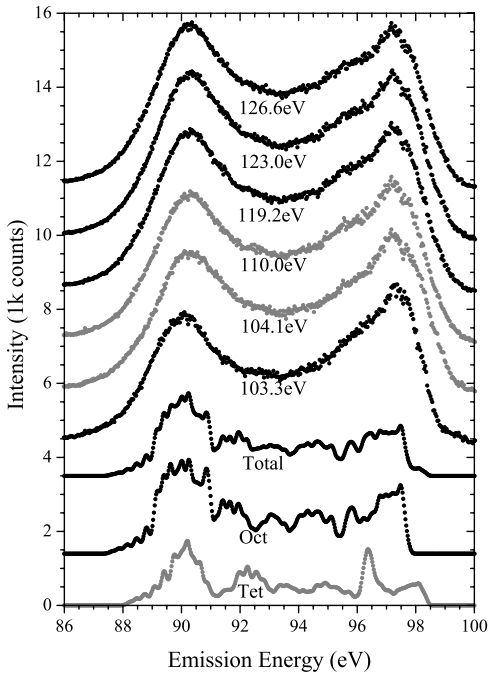

Figure 4.13: γ-Si_3N_4 Si $L_{2,3}$ emission measured for energies indicated in Figure 4.12.

Figure 4.12 shows a more detailed absorption spectrum for γ-Si_3N_4, as well as calculated XANES for comparison. The two lowest XANES spectra show the contribution of the absorption spectra from each non-equivalent site. Above them is the total spectrum, which is a weighted average of the two based on a 2:1 octahedral-to-tetrahedral site density ratio. Discounting the excitonic peaks, the experimental data are in good agreement with the total calculated Si LPDOS. Any disagreement between the two spectra is largely a result of spectral broadening and the insufficiencies of the theoretical techniques. This can be verified by observing the sharp nature of the excitonic peaks, which provide a better indication of instrumentation limits. The close agreement of measured and calculated data makes the use of calculated, site-specific XANES differences viable.

Figure 4.13 shows the resonant Si $L_{2,3}$ XES emission spectra excited at different photon energies for γ-Si_3N_4, as well as the calculated LPDOS for Si states with s and d symmetry for each of the non-equivalent sites. The octahedral silicon LPDOS has been shifted 0.6 eV to lower energy with respect to tetrahedral silicon LPDOS to account for the total energy of the system with a missing core (2p) electron. The XES excitation energies are shown as arrows in Figure 4.12. These energies were chosen based on high absorption probability and a significant difference in site-specific XANES. All of the spectra have been scaled down so that the intensities of the spectra are equivalent at 91 eV where the site-specific LPDOS are roughly equivalent. By comparing tetrahedral and octahedral XANES spectra in Figure 4.12, the emission spectra have been broken into two groups based on the primary contributor to emission. Grey spectra (110.0 eV and 104.1 eV) are produced by exciting primarily tetrahedral silicon sites while black spectra are a result of emission from primarily octahedral silicon sites.

Very little dispersion is observed in γ-Si_3N_4 spectral. This is advantageous, as any dispersion in the spectra would overlap the effects of non-equivalent sites. Only emission spectra for the excitonic peaks, at 103.3 eV and 104.1 eV show a measurable difference, which is contributed to the effects of non-equivalent sites.

The two excitonic peaks in Figure 4.12 are each considered a different non-equivalent site. This is because they are separated by 0.6 eV, which is identical to the total energy difference of the system with a core hole in octahedral and tetrahedral sites. Since the excitonic peaks are very narrow, they provide a point where each site can be excited with a high degree of exclusivity. This is reflected in the shift in the high-energy onset edges of these two emission spectra with respect to those excited within the rest of the XAS

spectrum. This shift is expected as the excited octahedral or tetrahedral silicon is predicted to have a different overall energy, and therefore different energy onset.

It should be noted that the 0.6 eV energy shifted is also the energy shift for spin-orbit splitting in Si. It has been suggested that the two excitonic peaks are simply derived from a single spin-orbit split state. It is our belief that while this theory is quite viable, it does not entirely explain spectral differences between emission spectra from these two excitonic states and that the spectra are also influenced by differences in the non-equivalent sites. This is derived by examining the spectral differences directly.

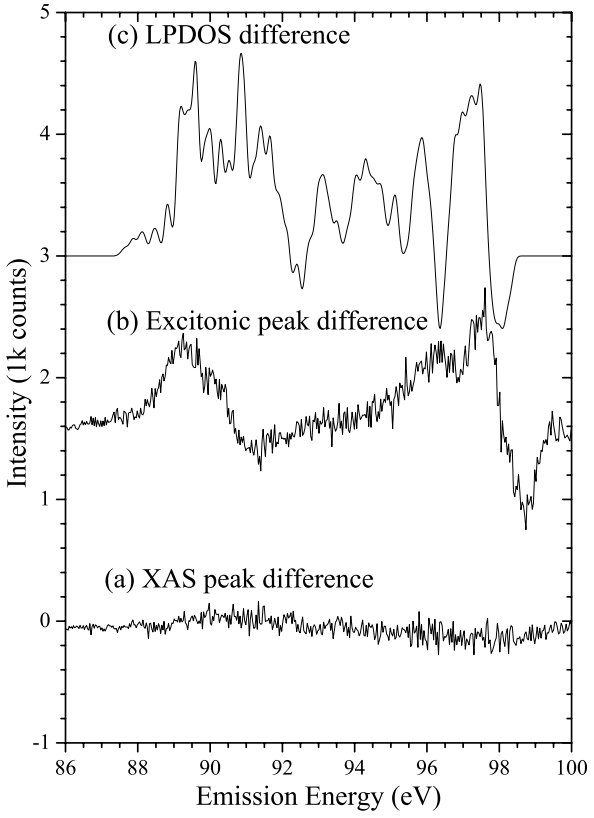

Figure 4.14: Difference spectra for comparison of emission from non-equivalent sites in γ-Si_3N_4.[60]

Since the dispersion of these spectra is nearly impossible to estimate with the naked eye, difference spectra were created. This is an unusual approach to use in XES because emission spectra inherently suffer from low count rates and therefore difference spectra would have poor measurement statistics. Figure 4.14 shows the difference spectra for two sets of non-equivalent site spectra, as compared to the LPDOS difference of the non-equivalent sites. Difference spectra are created by subtracting two scaled spectra, octahedral minus tetrahedral, and thereby accentuating the differences between them. Figure 4.14(a) shows the difference between the two emission spectra that were chosen to represent the measured XES spectra beyond the excitation peaks with the highest degree of tetrahedral or octahedral exclusivity (corresponding to spectra in Figure 4.13 excited at 110.0 and 119.2 eV), based on the calculated XANES. The difference spectrum of the two non-excitonic emission spectra provides little insight into the unique properties of the non-equivalent sites. Although some structure can be seen, there is not enough difference to make a reasonable conclusion.

Figure 4.14(b) shows the difference spectra of the two excitonic peaks (spectra in Figure 4.13 excited at 103.3 and 104.1 eV). The excitonic peaks are very sharp and provide nearly exclusive emission spectra. The difference spectrum of the two excitonic emission spectra is well defined, and shows a definite correlation with the LPDOS difference. The onset of the high-energy peak is at a higher energy for the tetrahedral component, producing a negative peak in the difference spectrum. The rest of the spectrum is primarily dominated by octahedral component, seen as two positive peaks. The sharp downturn in the high-energy peak is due to a peak in 3d tetrahedral LPDOS, and is much less pronounced in the experimental spectrum. Good agreement between the

experimental and calculated difference spectra provides strong evidence that properties of individual non-equivalent sites can be obtained by this method.

4.8 Band Gap

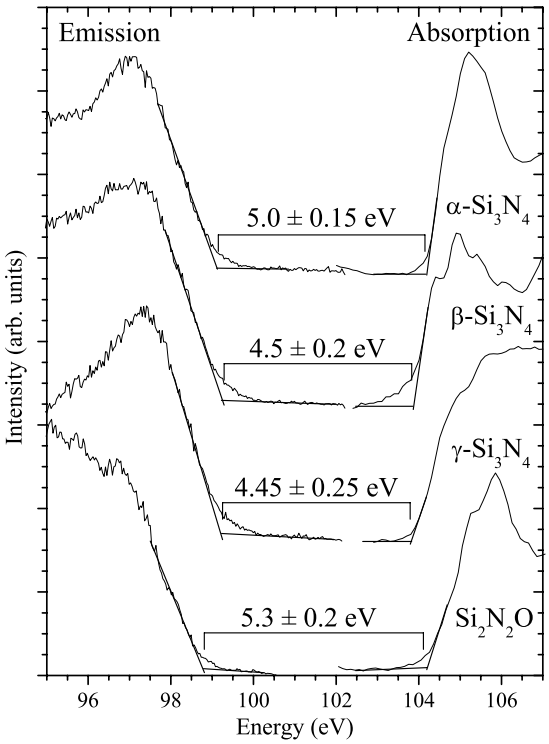

Figure 4.15: Band gap measurements using combined Si $L_{2,3}$ XAS/XES spectra near the Fermi level.

X-ray emission probes the density of electronic states at the top of the valence band. X-ray absorption measures the density of states at the bottom of the conduction band. By combining these two spectra on the same energy scale, the band gap can be measured. The Si $L_{2,3}$ emission and absorption spectra for each material are displayed on the same energy scale in Figure 4.15 along with the measured band gaps.

Table 4.1: Calculated and measured Si $L_{2,3}$ band gaps compared for each material.

Material	α-Si_3N_4	β-Si_3N_4	γ-Si_3N_4	Si_2N_2O
E_{Gap} calculated (eV)	4.63[12]	4.96[12]	3.45[23]	5.20[12]
E_{Gap} measured (eV)	5.0 ± 0.15	4.5 ± 0.2	4.45 ± 0.25	5.3 ± 0.2

The calculated and measured band gap for each material is listed in Table 4.1. Most of the calculated band gaps are smaller than the measured band gaps, which is to be expected since the DFT calculations underestimate the band gap value.[23] However, the calculated band gap for β-Si_3N_4 is larger then the measured band gap. The reason for this is unclear. Most of the calculated values are a reasonable approximation of the measured band gap, but do not vary as widely as the predicted values. The calculations show almost a 2 eV spread in band gap values, while the measured band gaps fit within a range of less than 1 eV.

While this method is not the best for determining band gaps, it is still a very useful measurement. Traditional reflectance band gap measurements require single crystal samples of sufficient surface area to focus light on. Many of the systems we deal with can only be produced in polycrystalline form, and can therefore not be measured using reflectance. The XES/XAS method can be used on any materials that have measurable absorption and emission spectra, which includes polycrystalline and amorphous samples. However, it is important to understand what effects can alter this measured band gap, which will give an idea of the accuracy of these measurements.

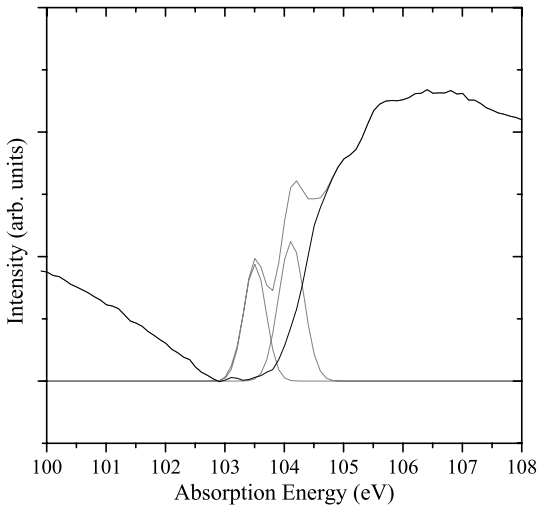

Figure 4.16: Excitonic peak removal in γ-Si_3N_4

γ-Si_3N_4 contains sharp excitonic peaks at the onset of the absorption spectrum. These peaks exist within the band gap, before the onset of the absorption spectrum due to the conduction band. In order to identify the conduction band onset correctly, these excitonic peaks must be removed. A gaussian peak-fitting tool was used to fit the entire absorption spectra focussing on the near edge in detail. Two peaks were identified as excitonic peaks (shown in grey in Figure 4.16) and subsequently subtracted from the rest of the spectrum. The resulting spectrum exhibits a sharp onset much like the other materials, which can be extrapolated to determine the conduction band onset.

Instrumental accuracy will affect the measured band gap. In order to determine the band gap spectra from two different sources must be gathered each with its own set of errors. These errors can be broken into three categories: an absolute energy shift in the spectra, a relative energy shift between the two spectra, and relative energy shifts over the range of the spectra.

The absolute error is defined by the energy error of the measurement when compared to known values. In order to measure this, the spectra are compared to previously published results. A feature is chosen that exists in both our results and published results that can be pinpointed in energy as accurately as possible. The difference in energy of our spectra to previously documented values is the absolute error.

The relative energy shift is a measure of the misalignment of the two energy scales (absorption and emission) for each material. To correct for this energy shift, a measurement is taken at a known energy and the two energy scales must be shifted so that this known energy is the same for both spectra. This is accomplished by using the elastic peak from the monochromator reflected off the sample. The monochromator is set to a predetermined energy (preferably near the onset of the emission spectra). Since the energy scale of the absorption spectra are determined by the energy produced by the monochromator, by adjusting the energy scale of the emission spectrum so that the elastic peak is at the same energy as the monochromator, the two energy scales are aligned.

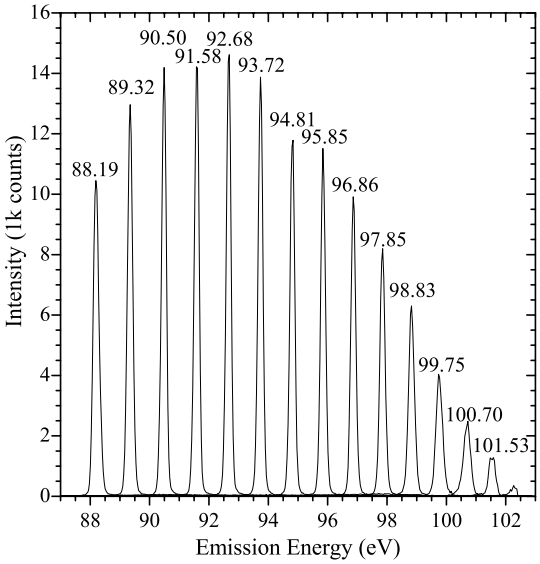

Figure 4.17: Relative energy shifting over the Si $L_{2,3}$ emission energy range.

The reason for choosing a point near the onset of the emission spectrum is to minimize the relative energy shifts over the range of the spectra. As the monochromator scans through the range of the absorption spectra, there will be a small difference between the x-ray beam's reported energy and the actual peak photon energy. In addition, although calibrated carefully, there are small errors in the energy assignment of channels on the spectrometer's MCD. These variations in the energy scale have been measured by measuring the elastic peak when the monochromator is shifted in 1 eV increments. Figure 4.17 shows the reflected elastic peak of the monochromator when the monochromator is set to 88-102 eV in 1 eV increments. The actual measured peak location is displayed above each peak. From this data, we can conclude that the energy scale shifts as much as 0.7 eV over the emission window. However, by calibrating the relative energy scale at the onset of the emission spectrum this variation is minimized with respect to band gap measurements.

Spin-orbit splitting will act to reduce the band gap for Si $L_{2,3}$ spectra. The spin-orbit interaction separates the L_2 and L_3 transition energies, causing two identical overlapping spectra separated by ~0.5 eV. Since the band gap is defined as the energy between the highest energy occupied and lowest energy occupied states, this effect will reduce the measured band gap by ~0.5 eV.

The presence of the core hole causes energy shifts in the absorption and emission spectra. Core hole interaction affects the onset energy of both absorption and emission spectra independently, causing a shift in the measured band gap. While changes due to the core hole are impossible to measure directly using x-ray spectra, calculations predict that core hole effects will reduce the band gap by ~0.5 eV in γ-Si_3N_4.

Since we are dealing with a polycrystalline material, there is a possibility for quantum confinement to affect the band gap. A paper by Luning et al[71] very clearly shows how the band gap can be affected by crystal size. As the crystal becomes smaller, the valence band edge migrates to lower energies, which effectively increases the band gap. This study was done on CdS crystals, but a similar study of quantum confinement in Si nano-particles shows a band gap widening of 0.26 eV (VB: -0.2 eV, CB: +0.06 eV) for 3.2 nm Si particles compared to crystalline Si.[4] Extrapolating the data, we can expect a maximum total shift of VB and CB edges of much less than 0.2 eV (for particles of 10 nm size) for our 10-50 nm γ-Si_3N_4 particles which is therefore neglected.

Phonon effects in polar materials have been found to cause spectral broadening as well as a shift of the occupied states to lower energies.[72] This effect is most apparent in ionically bonded SiO_2, but nearly zero in covalently bonded Si. Since Si_3N_4 and Si_2N_2O are primarily covalently bonded materials, the effects of phonon interactions will also be minimal.

Broadening factors will obviously reduce the measured band gap compared to the theoretical band gap determined from raw LPDOS. Broadening causes a “tail” to appear on each of the spectra. The first reaction for determining the band gap would be to remove all broadening of the system in order to determine the energy difference between the top of the valence band and the bottom of the conduction band. However, when the band gap is used in electronics we are actually interested in the energy of a photon required to excite an electron from the top of the valence band to the bottom of the conduction band. The excited electron will have a finite lifetime within the excited state,

therefore causing some lifetime broadening. The hole created when the electron is excited also has a finite lifetime, which also causes lifetime broadening. Therefore, when measuring the band gap, we want to remove the core hole lifetime broadening and the instrumental broadening but leave the final states lifetime broadening alone.

Then next question is how to remove the broadening. There are many different approaches to removing broadening, including deconvolution and fitting. For this analysis, we chose a simple straight-line approach. All of the spectra have an onset slope that consists of a straight slope followed by a tail. Our approach uses a straight line that follows the slope of the straight portion of the onset and another that follows the noise floor. The point where the two lines cross is considered the onset energy. The band gap is therefore measured as the energy difference of the two onsets. The errors stated in Figure 4.15 are therefore an estimate of the uncertainty associated with measuring the band gap using this method.

5 CONCLUSION

Soft x-ray spectroscopy is a powerful tool for analyzing solid-state materials. It provides insights into the electronic structure of a material that would otherwise be unobtainable. This paper presents results and analysis of spectroscopic data of three phases of Si_3N_4 and Si_2N_2O by comparing these results to calculated data.

Sharp peaks in the near edge Si $L_{2,3}$ absorption spectra were observed, and attributed to the localization of electron states surrounding Si atoms. These states exist within the delocalized conduction band but are highly localized around the Si nucleus. We have also shown that Si conduction band states depend primarily on the local coordination of the

nucleus, regardless of how it arranges in the crystal lattice. Conversely, N K absorption spectra appear to depend on long-range order of the material, whereby spectra of N atoms in an amorphous material produce featureless spectra compared to their polycrystalline counterpart.

Analysis of the Si $L_{2,3}$ emission spectra for these materials demonstrates hybridization of s and p orbital symmetry, producing an sp^3 tetrahedral bonding arrangement. Octahedral Si in γ-Si_3N_4 goes one step further by including hybridization of Si d states into the bonding states. This creates what could be called an sp^3d hybridized state. An sp^2/sp^3 bonding symmetry is also observed for N sites, but cannot be attributed to s-p hybridization since the calculated LPDOS shows only p symmetry. Comparing the Si spectra to N K emission spectra suggests the existence of a p-dπ interaction between Si and N. This interaction, along with the nearest neighbour N-N interaction is thought to cause this deformed bonding structure.

O K emission and absorption spectra have been presented for Si_2N_2O, which show the highly localized nature of O electrons. The spectra measured were nearly identical to similar spectra measured on entirely amorphous Si_2N_2O as well as SiO_2. O sites also exhibit a deformed bonding structure, which is attributed to a mixture of Si-O p-dπ interaction and nearest neighbour O-O interaction.

An analysis was done on Si $L_{2,3}$ spectra of γ-Si_3N_4 to determine if the contribution of the emission spectra from two non-equivalent sites could be determined. By exploiting highly localized excitonic peaks, emission that favoured one non-equivalent site was measured. By comparing the differences between spectra measured for each non-

equivalent site to those of calculated spectra, unique attributes could be extracted. While this conclusion does not directly provide new information about the γ-phase of Si_3N_4, it does show that the method is feasible and can be used for other materials.

Finally, by combining emission and absorption on the same energy scale, the band gaps for each material were measured, many for the first time. The measured gaps showed a narrower range of values than those predicted by calculated models.

BIBLIOGRAPHY

1. Mullaney, J.F., *Optical Properties and Electronic Structure of Solid Silicon.* Physical Review, 1944. **66**(11): p. 326-339.
2. Eisebitt, S., et al., *Resonant Inelastic Soft X-ray Scattering at the Si L_3 edge: Experiment and Theory.* Journal of Electron Spectroscopy and Related Phenomena, 1998. **93**(1-3): p. 245-250.
3. Eisebitt, S., et al., *Soft-X-ray Fluorescence of Porous Silicon: Electronic Structure of Si Nanostructures.* Europhysics Letters, 1997. **37**(2): p. 133-138.
4. van Buuren, T., et al., *Changes in the Electronic Properties of Si Nanocrystals as a Function of Particle Size.* Physical Review Letters, 1998. **80**(17): p. 3803-3806.
5. Eisebitt, S., et al., *Quantum Confinement Effects in the Soft X-ray Fluorescence Spectra of Porous Silicon Nanostructures.* Solid State Communications, 1996. **97**(7): p. 549-552.
6. Hardie, D. and Jack, K.H., *Crystal Structures of Silicon Nitride.* Nature, 1957. **180**(4581): p. 332-333.
7. Vassiliou, B. and Wilde, F.G., *Hexagonal Form of Silicon Nitride.* Nature, 1957. **179**(4556): p. 435-436.
8. Turkdogan, E.T., Bills, P.M., and Tippett, V.A., *Silicon Nitride: Some Physio-Chemical Properties.* Journal of Applied Chemistry, 1958. **8**: p. 333.
9. Tsukajima, J., et al., *Electron Energy Loss Fine Structure Measurements of Silicon Nitride Films.* Thin Solid Films, 1996. **282**(1-2): p. 318-320.
10. Wang, Q.L., Yan, Y.F., and Wang, R.H., *Convergent-Beam Electron Diffraction Study of Structure of β-Silicon Nitride.* Physica Status Solidi a-Applied Research, 1996. **155**(2): p. 289-297.
11. Zhao, G.L. and Bachlechner, M.E., *Electronic Structure and Charge Transfer in α- and β-Si_3N_4 and at the Si(111)/Si_3N_4(001) Interface.* Physical Review B, 1998. **58**(4): p. 1887-1895.
12. Xu, Y.N. and Ching, W.Y., *Electronic-Structure and Optical-Properties of α-Phase and β-Phase of Silicon-Nitride, Silicon Oxynitride, and with Comparison to Silicon Dioxide.* Physical Review B, 1995. **51**(24): p. 17379-17389.
13. Ren, S.Y. and Ching, W.Y., *Electronic-Structures of β-Silicon and α-Silicon Nitride.* Physical Review B, 1981. **23**(10): p. 5454-5463.
14. Carson, R.D. and Schnatterly, S.E., *Valence-Band Electronic-Structure of Silicon-Nitride Studied with the Use of Soft-X-Ray Emission.* Physical Review B, 1986. **33**(4): p. 2432-2438.
15. Clancy, W.P., *Limited Crystallographic and Optical Characterization of α and β Silicon-Nitride.* Microscope, 1974. **22**(4): p. 279-315.
16. Jack, K.H., *Prospects for Nitrogen Ceramics.* Silicon Nitride 93, 1994. **89-9**: p. 345-349.
17. Gnesin, G.G. and Yaroshenko, V.P., *Structure and Characteristics of Si_3N_4-Based Ceramic Cutting Tools.* Silicon Nitride 93, 1994. **89-9**: p. 737-741.
18. Morgan, P.E.D., *α-β-Si_3N_4 Question.* Journal of Materials Science, 1980. **15**(3): p. 791-793.

19. Luongo, J.P., *Infrared Characterization of Alpha-Crystalline and Beta-Crystalline Silicon-Nitride.* Journal of the Electrochemical Society, 1983. **130**(7): p. 1560-1562.
20. Senemaud, C., et al., *Electronic-Structure of Silicon-Nitride Studied by Both Soft-X-Ray Spectroscopy and Photoelectron-Spectroscopy.* Journal of Applied Physics, 1993. **74**(8): p. 5042-5046.
21. Zerr, A., et al., *Synthesis of Cubic Silicon Nitride.* Nature, 1999. **400**(6742): p. 340-342.
22. Ching, W.Y., et al., *Theoretical Prediction of the Structure and Properties of Cubic Spinel Nitrides.* Journal of the American Ceramic Society, 2002. **85**(1): p. 75-80.
23. Ching, W.Y., Mo, S.D., and Oyuang, L., *Electronic and Optical Properties of the Cubic Spinel Phase of c-Si_3N_4, c-Ge_3N_4, c-$SiGe_2N_4$, and c-$GeSi_2N_4$.* Physical Review B, 2001. **63**(24): p. art. no. 245110.
24. Jiang, J.Z., et al., *Hardness and Thermal Stability of Cubic Silicon Nitride.* Journal of Physics-Condensed Matter, 2001. **13**(22): p. L515-L520.
25. Tanaka, I., et al., *Hardness of Cubic Silicon Nitride.* Journal of Materials Research, 2002. **17**(4): p. 731-733.
26. Jiang, J.Z., et al., *Compressibility and Thermal Expansion of Cubic Silicon Nitride.* Physical Review B, 2002. **65**(16): p. art. no. 161202.
27. Zhang, M., et al., *High-Resolution Transmission Electron Microscopy of Cubic Si_3N_4.* Journal of Applied Physics, 2000. **88**(5): p. 3070-3072.
28. Sekine, T., Tansho, M., and Kanzaki, M., *^{29}Si Magic-Angle-Spinning Nuclear-Magnetic-Resonance Study of Spinel-Type Si_3N_4.* Applied Physics Letters, 2001. **78**(20): p. 3050-3051.
29. Tanaka, I., et al., *Electron Energy Loss Near-Edge Structures of Cubic Si_3N_4.* Applied Physics Letters, 2001. **78**(15): p. 2134-2136.
30. Poon, C.O., et al., *Improved Performance and Stability of Organic Light-Emitting Devices with Silicon Oxy-Nitride Buffer Layer.* Applied Physics Letters, 2003. **83**(5): p. 1038-1040.
31. Eldada, L., *Optical Communication Components.* Review of Scientific Instruments, 2004. **75**(3): p. 575-593.
32. McGuinness, C., et al., *Electronic Structure of Thin Film Silicon Oxynitrides Measured using Soft X-ray Emission and Absorption.* Journal of Applied Physics, 2003. **94**(6): p. 3919-3922.
33. Carlisle, J.A., et al., *Soft-X-ray Fluorescence Studies of Solids.* Journal of Electron Spectroscopy and Related Phenomena, 1999. **103**: p. 839-845.
34. Krause, M.O., *Atomic radiative and radiationless yields for K and L shells.* Journal of Physical and Chemical Reference Data, 1979. **8**(2): p. 307-327.
35. Rubensson, J.E., et al., *It's always a one-step process.* Applied Physics a-Materials Science & Processing, 1997. **65**(2): p. 91-96.
36. Ching, W.Y., *Theoretical-Studies of the Electronic-Properties of Ceramic Materials.* Journal of the American Ceramic Society, 1990. **73**(11): p. 3135-3160.
37. Vonbarth, U. and Grossmann, G., *Dynamical Effects in X-Ray-Spectra and the Final-State Rule.* Physical Review B, 1982. **25**(8): p. 5150-5179.

38. Krause, M.O. and Oliver, J.H., *Natural Widths of Atomic K-Levels and L-Levels,Kα X-Ray-Lines and Several KLL Auger Lines.* Journal of Physical and Chemical Reference Data, 1979. **8**(2): p. 329-338.
39. Goodings, D.A. and Harris, R., *Calculations of X-Ray Emission Bands of Copper Using Augmented Plane Wave Bloch Functions.* Journal of Physics Part C Solid State Physics, 1969. **2**(10): p. 1808.
40. *High Resolution and Flux for Materials and Surface Science • Beamline 8.0.1.* 2003, Available from http://www-als.lbl.gov/als/.
41. *Soft X-Ray Fluorescence (SXF) Spectrometer • Beamline 8.0.1.* 2003, Available from http://www-als.lbl.gov/als/.
42. Jia, J.J., et al., *First Experimental Results from IBM/Tenn/Tulane/LLNL/LBL Undulator Beamline at the Advanced Light-Source.* Review of Scientific Instruments, 1995. **66**(2): p. 1394-1397.
43. Henke, B.L., Gullikson, E.M., and Davis, J.C., *X-Ray Interactions - Photoabsorption, Scattering, Transmission and Reflection at E=50-30,000 eV, Z=1-92 (Vol 54, Pg 181, 1993).* Atomic Data and Nuclear Data Tables, 1993. **55**(2): p. 349-349.
44. Ching, W.Y., Mo, S.D., and Chen, Y., *Calculation of XANES/ELNES Spectra of All Edges in Si_3N_4 and Si_2N_2O.* Journal of the American Ceramic Society, 2002. **85**(1): p. 11-15.
45. Ching, W.Y., Ouyang, L.Z., and Gale, J.D., *Full Ab Initio Geometry Optimization of All Known Crystalline Phases of Si_3N_4.* Physical Review B, 2000. **61**(13): p. 8696-8700.
46. Borgen, O. and Seip, H.M., *Crystal Structure of β-Si_3N_4.* Acta Chemica Scandinavica, 1961. **15**(8): p. 1789.
47. Rosenflanz, A., *Silicon Nitride and SiAlON Ceramics.* Current Opinion in Solid State & Materials Science, 1999. **4**(5): p. 453-459.
48. Arnett, P.C. and Yun, B.H., *Silicon-Nitride Trap Properties as Revealed by Charge-Centroid Measurements on MNOS Devices.* Applied Physics Letters, 1975. **26**(3): p. 94-96.
49. Hisamoto, D., et al., *FinFET - A Self-Aligned Double-Gate MOSFET Scalable to 20 nm.* Ieee Transactions on Electron Devices, 2000. **47**(12): p. 2320-2325.
50. Malkow, T., *Critical Observations in the Research of Carbon Nitride (vol 292, pg 112, 2000).* Materials Science and Engineering a-Structural Materials Properties Microstructure and Processing, 2001. **302**(2): p. 309-324.
51. Sekine, T., et al., *Shock-Induced Transformation of β-Si_3N_4 to a High-Pressure Cubic-Spinel Phase.* Applied Physics Letters, 2000. **76**(25): p. 3706-3708.
52. Sekine, T., *Shock Synthesis of Cubic Silicon Nitride.* Journal of the American Ceramic Society, 2002. **85**(1): p. 113-116.
53. Sekine, T. and Mitsuhashi, T., *High-Temperature Metastability of Cubic Spinel Si_3N_4.* Applied Physics Letters, 2001. **79**(17): p. 2719-2721.
54. Brosset, C. and Idrested, I., *Crystal Structure of Silicon Oxynitride Si_2N_2O.* Nature, 1964. **201**(492): p. 1211.
55. Wiech, G. and Simunek, A., *Analysis of the Electronic and Local-Structure of Amorphous SiN_xH Alloy-Films in Terms of SiK, SiL, and NK X-Ray-Emission Bands.* Physical Review B, 1994. **49**(8): p. 5398-5405.

56. Brown, F.C., Bachrach, R.Z., and Skibowski, M., *$L_{2,3}$ Threshold Spectra of Doped Silicon and Silicon-Compounds.* Physical Review B, 1977. **15**(10): p. 4781-4788.
57. Nithianandam, V.J. and Schnatterly, S.E., *Soft-X-Ray Emission-Spectroscopy Study of the Electronic-Structure of Nonstoichiometric Silicon-Nitride.* Physical Review B, 1987. **36**(2): p. 1159-1167.
58. Obrien, W.L., et al., *Soft-X-Ray Emission Insulators - Spectator Versus Normal Emission.* Physical Review Letters, 1993. **70**(2): p. 238-241.
59. Iqbal, A., et al., *Electronic-Structure of Silicon-Nitride and Amorphous-Silicon Silicon-Nitride Band Offsets by Electron-Spectroscopy.* Journal of Applied Physics, 1987. **61**(8): p. 2947-2954.
60. Leitch, S., et al., *Properties of Non-Equivalent Sites and Bandgap of Spinel-Phase Silicon Nitride.* Journal of Physics-Condensed Matter, 2004. **16**(36): p. 6469-6476.
61. Gu, H., et al., *A Quantitative Approach for Spatially-Resolved Electron-Energy-Loss Spectroscopy of Grain-Boundaries and Planar Defects on a Subnanometer Scale.* Ultramicroscopy, 1995. **59**(1-4): p. 215-227.
62. Obrien, W.L., et al., *Resonant Absorption and Emission from Localized Core-Hole States in Al_2O_3 and SiO_2.* Nuclear Instruments & Methods in Physics Research Section B-Beam Interactions with Materials and Atoms, 1991. **56-7**: p. 320-323.
63. Paloura, E.C., et al., *Microstructural Characterization of Stoichiometric Buried Si_3N_4 Films.* Nuclear Instruments & Methods in Physics Research Section B-Beam Interactions with Materials and Atoms, 1996. **113**(1-4): p. 227-230.
64. Paloura, E.C., *Evolution of Defect-Related Structure in the X-ray Absorption Spectra of Buried SiN_x Films.* Applied Physics Letters, 1997. **71**(22): p. 3209-3211.
65. Liu, A.Y. and Cohen, M.L., *Structural-Properties and Electronic-Structure of Low-Compressibility Materials - β-Si_3N_4 and Hypothetical β-C_3N_4.* Physical Review B, 1990. **41**(15): p. 10727-10734.
66. Robertson, J., *The Electronic-Properties of Silicon-Nitride.* Philosophical Magazine B-Physics of Condensed Matter Statistical Mechanics Electronic Optical and Magnetic Properties, 1981. **44**(2): p. 215-237.
67. Haouari, M., et al., *Electron-Paramagnetic-Resonance Study of 5-Coordinated Cu2+ Ethylenediammonium Copper(Ii) Diphosphate Monohydrate.* Journal of Physics-Condensed Matter, 1995. **7**(15): p. 3023-3032.
68. Doualan, J.L., et al., *Energy-Levels of the Laser Active Er3+ Ion in Each of the 2 Crystallographic Sites of Yttrium Orthosilicate.* Journal of Physics-Condensed Matter, 1995. **7**(26): p. 5111-5126.
69. Vergara, I., et al., *Nonequivalent Chromium Sites in Natural Eosphorite.* Chemical Physics Letters, 1991. **186**(6): p. 495-500.
70. Guo, J.H., et al., *Electronic-Structure of $La_{2-x}Sr_xCuO_4$ Studied by Soft-X-Ray-Fluorescence Spectroscopy with Tunable Excitation.* Physical Review B, 1994. **49**(2): p. 1376-1380.
71. Luning, J., et al., *Soft X-ray Spectroscopy of Single Sized CdS Nanocrystals: Size Confinement and Electronic Structure.* Solid State Communications, 1999. **112**(1): p. 5-9.

72. Obrien, W.L., et al., *Phonon Relaxation in Soft-X-Ray Emission of Insulators.* Physical Review B, 1993. **47**(1): p. 140-143.
73. Hohenberg, P. and Kohn, W., *Inhomogeneous Electron Gas.* Physical Review B, 1964. **136**(3B): p. B864.
74. Kohn, W. and Sham, L.J., *Self-Consistent Equations Including Exchange and Correlation Effects.* Physical Review, 1965. **140**(4A): p. 1133.
75. Cottenier, S., *Density Functional Theory and the Family of (L)APW-methods: a Step-by-Step Introduction*. 2002, Instituut voor Kern- en Stralingsfysica: K.U.Leuven, Belgium (to be found at http://www.wien2k.at/reg_user/textbooks).

APPENDICES

A Density Functional Theory

Both the OLCAO calculations from Wai-Yim Ching and the Wien2k calculations discussed in Appendix B use density functional theory to calculate the electron density for materials. Density functional theory is a method of solving the many body problem of electrons within a crystal.[73, 74] Instead of attempting to solve the Schrödinger equation for all electrons within the system, DFT describes the system in terms of a single electron density functional $\rho(\mathbf{r})$, where $\mathbf{r}$ is the location in space. The total energy of the system is then defined as:

$$E_{tot}[\rho(\boldsymbol{r})]=T_s[\rho(\boldsymbol{r})]+E_{ee}[\rho(\boldsymbol{r})]+E_{Ne}[\rho(\boldsymbol{r})]+E_{xc}[\rho(\boldsymbol{r})]+E_{NN} \tag{A1}$$

Where T_s is the kinetic energy of the non-interacting electrons, E_{ee}, E_{Ne}, and E_{NN} are the coulombic electron-electron, electron-nucleus, and nucleus-nucleus interaction respectively, and E_{xc} is the energy due to exchange correlation. According to density functional theory, the system is exactly solved by finding an electron density that minimizes the total energy of the system. The general method of accomplishing this is to differentiate the right side of Equation A1 with respect to $\rho(\mathbf{r})$ and set it equal to zero, which results in the equation:

$$\int \rho(\boldsymbol{r})\left[v(\boldsymbol{r})+v_{ee}[\rho(\boldsymbol{r})]+v_{xc}[\rho(\boldsymbol{r})]+\frac{\partial T_s[\rho(\boldsymbol{r})]}{\partial \rho(\boldsymbol{r})}\right]d\boldsymbol{r}=0 \tag{A2}$$

where:

$$v_{xc} = \frac{\partial E_{xc}[\rho(\boldsymbol{r})]}{\partial \rho(\boldsymbol{r})} \tag{A3}$$

$$v_{ee}[\rho(\boldsymbol{r})] = \int \frac{\rho(\boldsymbol{r}')}{|\boldsymbol{r} - \boldsymbol{r}'|} d\,\boldsymbol{r}' \tag{A4}$$

For the calculation methods presented in this thesis, the local density approximation is used for v_{xc}. The local density approximation is a first order approximation of the exchange correlation based only on ρ(r), equivalent to exchange correlation of a homogeneous electron cloud.

By defining the electron density as a sum of orbitals:

$$\rho(\boldsymbol{r}) = \sum_i \rho_i |\varphi_i(\boldsymbol{r})|^2 \tag{A5}$$

Equation A2 can be rewritten:

$$-\nabla^2 \varphi_i(\boldsymbol{r}) + [v(\boldsymbol{r}) + v_{ee}(\boldsymbol{r}) + v_{xc}[\rho(\boldsymbol{r})]]\varphi_i(\boldsymbol{r}) = \epsilon_i \varphi_i(\boldsymbol{r}) \tag{A6}$$

This is a familiar form of the Schrödinger equation. The effective potential for this equation can be written:

$$v_{eff} = v(\boldsymbol{r}) + v_{ee}(\boldsymbol{r}) + v_{xc}[\rho(\boldsymbol{r})] \tag{A7}$$

Equations A5, A6 and A7 collectively are known as the Kohn-Sham equations and can be solved iteratively. The process is as follows:

1. Choose a set of $\varphi_i(\mathbf{r})$ and calculate $\rho(\mathbf{r})$.

2. Plug that into Equation A7 to get a value for v_{eff}.

3. Use that v_{eff} in Equation A6 to derive a new set of $\varphi_i(\mathbf{r})$.

4. Repeat until the system converges.

B Wien2k Calculations

All of the calculations used in this thesis have been provided by Prof. Wai-Yim Ching's group at the University of Missouri - Kansas City. However, many of the calculations shown in this thesis have also been repeated using a commercial program called Wien2k.[75] Wien2k uses the density functional theory discussed in Appendix A, but uses a different method than OLCAO. The method Wien2k uses is known as Linearized Augmented Plane Wave with Local Orbitals (LAPW+LO) method.[75] The LAPW+LO method divides the unit cell into two distinct regions: atomic spheres (labelled I in Figure B1) and the interstitial region (labelled II in Figure B1). Within the atomic spheres, the basis sets for the electron density that are made up of radial functions times spherical harmonics. In the interstitial region, the electronic density basis set is derived from a plane wave expansion. The initial electron density used for the iterative process is then found by solving for boundary conditions.

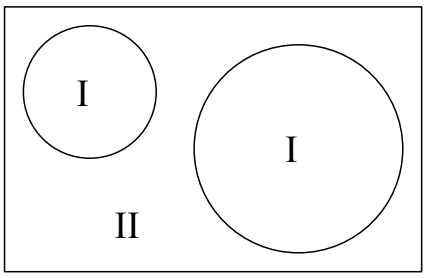

Figure B1: Partitioning of unit cell into atomic spheres (I) and interstitial region (II)

Figure B2 and Figure B3 show an example of the calculated LPDOS for Si s and d symmetry, and N p symmetry respectively. For each figure, the top spectrum shows the LPDOS using Prof. Ching's OLCAO method, and the bottom spectrum shows the same LPDOS using the Wien2k APW method. The two spectra in each set are very similar. In fact, the only reason for using Prof. Ching's calculations is for consistency. The Wien2k code does not directly have a method of developing a supercell and combining an LPDOS measurement, including the core hole, with the ground state LPDOS to produce a XANES spectrum. By using Prof. Ching's calculations throughout the manuscript, the consistency of results are assured.

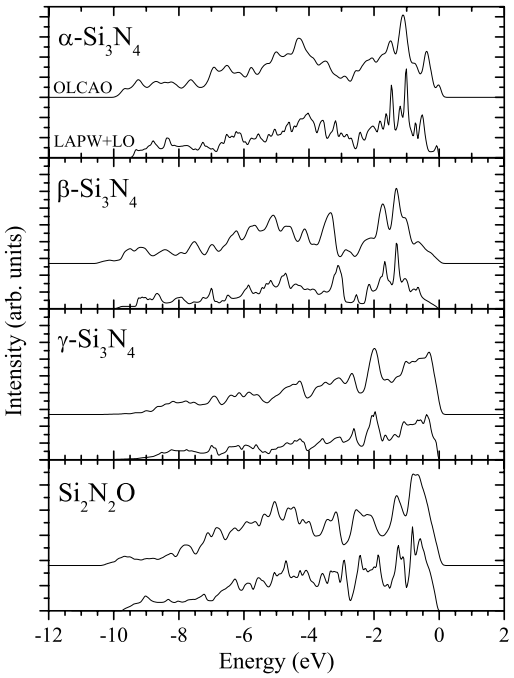

Figure B2: Comparison of N p symmetric LPDOS using two different calculations.

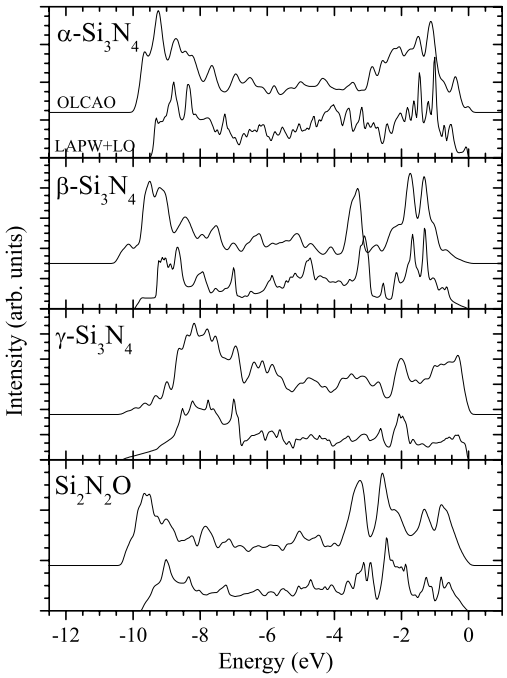

Figure B3: Comparison of Si s+d symmetric LPDOS using two different calculations.

C Absorption and Emission Spectra of Silicon and Silicon Ceramics

The four materials presented in this thesis are not the only silicon ceramics that have been measured using x-ray spectroscopy by our group. The emission spectra for nine silicon materials are presented in Figure C1. The absorption spectra taken for the same nine materials are presented in Figure C2. All of these spectra were obtained at Beamline 8.0.1 at the Advanced Light Source during various measurement sessions dating back to November 2002.

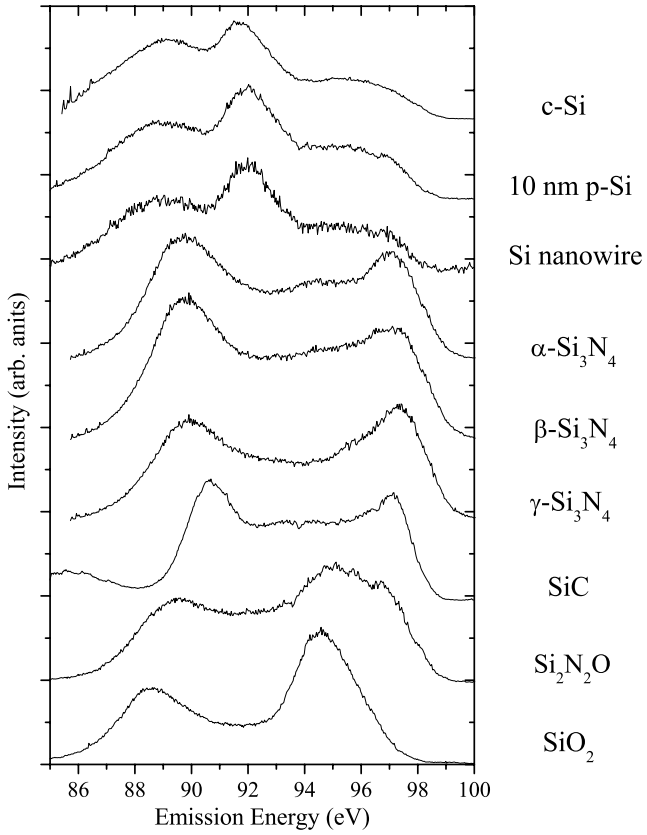

Figure C1: Si $L_{2,3}$ x-ray emission spectra of nine selected silicon materials.

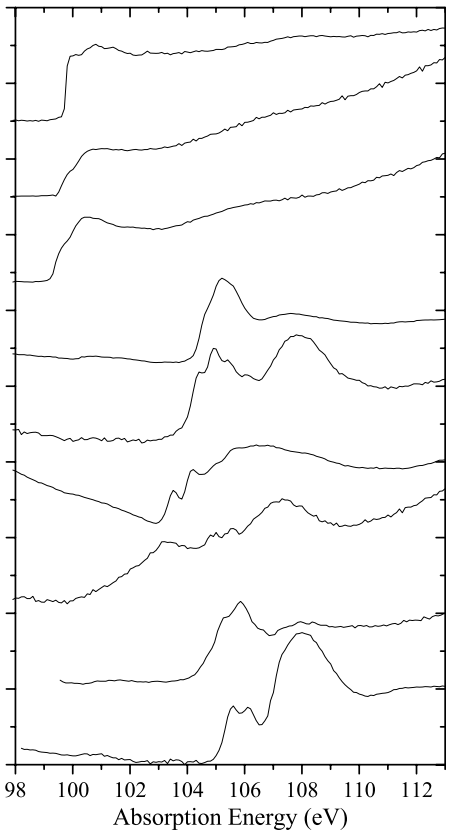

Figure C2: Si $L_{2,3}$ x-ray absorption spectra of nine selected silicon materials.

Results indicate two classes of materials within the nine samples, each with similar features among their respective spectra:

The top three spectra represent the pure silicon materials consisting of crystalline silicon, 10 nm porous silicon, and silicon nanowires. For emission, these spectra have a three-peak structure consisting of primarily s symmetry below 90 eV, hybridized p states exhibiting s symmetry between 90 eV and 94 eV, and non-bonded p and d symmetry above 94 eV. The absorption spectra have a spin-orbit split onset at ~100 eV that varies based on the quantum confinement of the crystal, consistent with previously documented results.[3-5]

The second class of materials is the silicon compound ceramics: α-Si_3N_4, β-Si_3N_4, γ-Si_3N_4, SiC, Si_2N_2O, and SiO_2. The emission spectra of these materials also exhibit three main features: s symmetry below 91 eV, non-bonding d symmetry above 93 eV, and hybridization with p symmetry between these two peaks. The location of the non-bonding d symmetry above 93 eV is based on the constituent elements that make up the material. For those materials containing oxygen (SiO_2 and Si_2N_2O), there is a peak at ~95 eV while those materials containing either nitrogen or carbon have a peak closer to ~97 eV. The location of these peaks is partially attributed to the interaction of these non-bonded states with neighbouring atoms as discussed in Sections 4.5 and 4.6. The absorption spectra for these materials exhibit fine structure below ~106 eV due to localization of Si states in that region, followed by the delocalized conduction band spectra.